Petroleum Science 23 (2026) 4296–4319

Contents lists available at ScienceDirect

Petroleum Science

journal homepage: www.keaipublishing.com/en/journals/petroleum-science

Original Paper

Investigation of tip leakage vortex instability and pressure pulsation characteristics in a vane-type multiphase pump

Hai-Gang Wen [a,b], Guang-Tai Shi [a,b,*], Wen-Juan Lv [a,b], Hao Qin [a,b]

[a] School of Energy and Power Engineering, Xihua University, Chengdu, 610039, Sichuan, China
[b] Key Laboratory of Fluid and Power Machinery (Xihua University), Ministry of Education, Chengdu, 610039, Sichuan, China

ARTICLE INFO

Article history:
Received 4 September 2025
Received in revised form
5 November 2025
Accepted 17 April 2026
Available online 22 April 2026

Edited by Min Li

Keywords:
Vane-type multiphase pump
Gas-liquid two-phase flow
Vortex evolution
Pressure pulsation
Experimental measurements
Computational fluid dynamics

ABSTRACT

As a key efficient transportation equipment in oil-gas extraction, vane-type multiphase pumps face significant performance limitations due to extensive vortex formation in flow channels. This study systematically investigates strong-weak vortex evolution in impellers using vorticity decomposition, secondary flow diagnosis, and rigid vorticity vector analysis. It examines how inlet gas volume fraction and flow rate affect axial vortices, circumferential vortices, and pressure pulsation. Key findings include: 1) Tip leakage vortex (TLV) in these pumps demonstrates fracture zones, leading to a proposed "front-middle-rear leakage vortex" structure; 2) TLV diffusion and shedding represent strong-weak vortex transitions, with mutual compression between front and middle vortices directly causing fracture; 3) Blade geometry correlates with fluid potential rotor enthalpy evolution to predict vortex patterns; 4) Circumferential vortex intensity increases with gas accumulation, while rapid axial vortex development influences gas distribution. Time-frequency analysis shows gas phase presence amplifies pressure pulsation and low-frequency disturbances in TLV regions, with axial vortex proliferation being the primary contributor to enhanced pulsation intensity. High-flow conditions intensify peripheral pulsations through unbroken TLV, while reduced front leakage vortex and rear vortex shedding attenuate pressure fluctuations.

1. Introduction

The global coastline and vast land areas are rich in oil and natural gas resources, making their efficient extraction an urgent priority. However, extracting these resources from deep-sea and inland underground locations is challenging and time-consuming. Selecting appropriate extraction and transportation equipment can significantly improve efficiency. Current equipment mainly includes screw pumps (Cao et al., 1999) and vane-type multiphase pumps (Cheng and Chen, 1999; Ling, 2000). Compared to conventional screw pumps, vane-type multiphase pumps offer advantages such as longer service life, easier maintenance, and higher transportation capacity. In particular, enclosed gathering and transportation technology has greatly simplified the transportation process, effectively reducing maintenance costs. The research and design of vane-type multiphase pumps have long been a focal point of study worldwide. Over the past decade, continuous optimization and improvements by researchers have led to significant performance enhancements (Yao et al., 2020).

However, there remain numerous challenges to be addressed in the practical operation of vane-type multiphase pumps, particularly the large-scale vortices that form in the flow channels of the pressure-boosting unit, which significantly impact pump performance (Zhang et al., 2014; Li et al., 2013; Ling, 2000). In a vane-type multiphase pump, the impeller is a rotating component, and there must be a certain gap between the blade tip and the inner wall, known as the tip clearance. The fluid leaking through this gap forms a jet driven by the pressure difference on both sides of the blade, which then interacts with the main flow and evolves into a TLV. The TLV not only intensifies unstable flow within the pump but also induces hazards such as cavitation, vibration, and noise. Additionally, secondary flows and leakage vortices in the flow channels collide, merge, and dissipate, leading to significant energy losses and further reducing the pump's work capacity and efficiency. Meanwhile, vortex-induced disturbances generate

* Corresponding author.
E-mail address: sgtaixh@mail.xhu.edu.cn (G.-T. Shi).
Peer review under the responsibility of China University of Petroleum (Beijing).

https://doi.org/10.1016/j.petsci.2026.04.031

noise, vibration, and intensified pressure pulsations in the pressure-boosting unit, profoundly affecting the safe and stable operation of the entire system. Therefore, it is essential to study the characteristics of unstable vortices and pressure pulsations in the flow channels.

From a theoretical research perspective, Nayak and Das (2021) and Wu et al. (2020) identified the physical foundations of unstable flows and provided detailed explanations regarding the velocity field theory of fluid parcels. Li et al. (2023) demonstrated that malignant cavitation serves as the primary cause of head reduction and operational instability in mixed-flow pumps by inducing increased energy dissipation and impairing impeller workload capacity. Ye et al. (2024) demonstrated that the stress blended eddy simulation model achieved superior accuracy in predicting the vortex core velocity field while maintaining computational efficiency for TLV analysis in axial liquid hydrogen pumps. Turgut and Daly (1987) demonstrated that shear flow within the flow field causes vortex deformation and explicitly stated that unstable flows in weak turbulence are associated with sinusoidal instability, while in strong turbulence, unstable flows manifest as vortices. Yu et al. (2020) pointed out that vorticity cannot precisely represent vortices. Due to the presence of strong shear forces in boundary regions that amplify vorticity, this does not align with the physical definition of vortices. Therefore, they concluded that high vorticity does not necessarily indicate strong vortex intensity. Gao et al. (2019); Liu et al. (2018) and Dong et al. (2019) proposed that a vortex must simultaneously satisfy six defining criteria: absolute strength, relative strength, rotational axis, vortex core center, vortex core size, and vortex boundary. They clearly demonstrated that second-generation vortex identification criteria fail to meet these requirements, whereas third-generation vortex identification methods can define the boundaries of rotational vortices based on the condition that the antisymmetric tensor exceeds the symmetric tensor, thereby avoiding contamination by shear vorticity. Lu and Gao (2003) employed a combination of helicity equations and vorticity to reveal that the time-varying rate of helicity in vortex structures within the flow field is closely related to the magnitude of vorticity. Scheeler et al. (2017) discovered that helical vortices exhibit twisted and coiled characteristics. Through experiments, they validated the helicity conservation theory in viscous fluids and noted that in real fluids, vortex rings mutually induce one another, causing their coiled characteristics to gradually weaken while the overall helicity remains conserved.

In experimental research, Long et al. (2024) demonstrated that cavitation development significantly altered the TLV structure and intensified pressure pulsation within the tip clearance region. Muthanna and Devenport (2004) conducted an in-depth study on the mean flow and turbulent kinetic energy downstream of a compressor cascade. They concluded that the turbulent kinetic energy of the blade wake vortex structure is generated by velocity gradients. Zhang et al. (2016) visualized experiments on vane-type multiphase pumps and found that a large number of vortices are generated in the guide vane flow passage. These vortices exhibit strong entrainment capacity and exacerbate gas-liquid separation. Liu et al. (2019) also noted that there are roughly four types of vortices in the impeller flow passage: leading-edge vortices, leakage vortices, separation vortices, and wake vortices. Shi et al., 2020a, 2020c summarized the characteristics of vortices such as separation vortices and leakage vortices in the tip clearance and experimentally observed the trajectory of leakage vortices. The high-speed PIV (Particle Image Velocimetry) technique used in these studies has been widely applied to observe flow patterns in the rim region, including various vortices such as wake vortices (Zhang et al., 2014, 2021). Using SPIV (Stereo Particle Image Velocimetry), Wu et al. (2021, 2012) observed leakage vortices induced by tip clearance in jet pumps and identified the formation of wake vortices near the blade trailing edge. Shi et al., 2020d captured the evolution of vortex motion in a swirl pump using high-speed cameras and demonstrated the trajectory of particles following vortex changes. Lee et al. (2020) employed velocity measurement and visualization techniques to study the wake characteristics of axial-flow turbines. They explicitly stated that the vortex intensity of wake vortices is a key factor determining the stability of the core region. Ma and Devenport (2006, 2007) investigated the influence of tip clearance on the unsteady characteristics of compressor tip leakage vortices and other vortex systems. The results showed that leakage vortices form shedding circulations near the trailing edge, which is one of the important transient evolution forms of TLV systems. Additionally, Liu et al. (2018) clearly identified wake vortices at the trailing edge of multiphase pump impeller blades through modal analysis and discussed the impact of unsteady flows such as vortices on flow blockage. Cavitation phenomena in the tip clearance region also present a challenging issue worthy of in-depth study. Shi et al. (2017) and Shen et al. (2021) focused on the adverse effects caused by cavitation flow in axial-flow pump tip leakage vortices. Under severe cavitation conditions, vertical cavitation vortices were captured in the wake region of leakage vortices, and their evolution process can be divided into three stages: generation, shedding, and dissipation. In terms of numerical simulation, Zhang et al. (2020) analyzed the influence of tip clearance on flow characteristics and performance in mixed-flow pumps through numerical calculations, summarizing the effects of clearance on channel vortices under different operating conditions. Their research revealed that leakage vortices and vorticity near the blade tip are significantly affected by clearance size and flow rate, with increased flow rate effectively improving vortex intensity and energy loss across different clearance sizes. Shu et al. (2021a,b) using the SST turbulence model, found that the gas phase substantially influences the generation and collapse of tip leakage vortices. Zhao et al. (2014) employed large eddy simulation (LES) to demonstrate a strong correlation between vortex shedding at hydrofoil trailing edges and cavitation intensity. Zhang et al. (2015a,b) identified that tip leakage vortices result from the interaction between leakage jets and the main flow. Yan et al. (2020) applying a population balance model to centrifugal pump simulations, observed that higher gas volume fractions lead to increased vortex generation on blade suction surfaces, exacerbating gas-liquid separation and potentially causing flow blockage. Zhao et al. (2022) numerically demonstrated that fewer vortex structures at impeller inlets/outlets correlate with higher mixed-flow pump efficiency. Shi et al. (2014) adopted vortex intensity methods to numerically analyze flow fields and leakage vortex trajectories in axial-flow pump tip regions. Their results showed that expanding operational flow ranges and larger tip clearances intensify leakage vortex entrainment, simultaneously elevating cavitation risks near blade walls. Zhang et al. (2015a,b) utilized large eddy simulation (LES) to demonstrate that leakage flows predominantly concentrate near blade trailing edges, forming tip wake vortices. These wake vortices migrate toward pressure surfaces of adjacent blades, interacting with walls to induce multiscale vortex generation. Li et al. (2022) highlighted that in rotary machinery, higher rotational speeds intensify channel vortices due to increased radial velocity gradients. Peng and Gregory (2015) combined PIV with numerical methods to prove blade-vortex interactions significantly modify vortex morphology and strength, with vortices splitting into fragments during collisions while gradually dissipating. Ji et al. (2020, 2021) identified that tip leakage vortices, secondary flow vortices, and stall vortices in mixed-flow pump impellers all contribute to high energy dissipation. Both intensity and scale of tip leakage vortices grow with clearance size, causing sharp rises in entropy generation. Furukawa et al. (1999) investigated transient vortex variations in compressors, observing vortex collapse in mid-to-rear tip regions that distorts local vortex structures, alters intensity, and amplifies pressure pulsation amplitudes.

Numerous scholars have investigated vortex mechanisms to enhance the performance of hydraulic rotating machinery and analyze the correlation between vortices and pressure pulsations. Among them, Li et al. (2019) demonstrated that the shape of the blade trailing edge significantly influences pressure fluctuations. Through numerical simulations, they found that modified blade trailing edges effectively reduce vortex intensity in the surrounding area, leading to a notable decrease in pressure pulsation amplitude within the pressure-boosting unit. Sun et al. (2020) highlighted the substantial impact of vortices generated at blade leading and trailing edges on centrifugal compressors. Adjusting blade thickness was proposed as an effective method to mitigate the influence of these vortices. Cui et al. (2020) employed LES to analyze the flow field in the rear section of a centrifugal pump impeller. Their results showed that modifying the blade trailing edge cutting angle effectively reduces unstable flow and helps lower pressure pulsations. Rashidi et al. (2016) reviewed applications for vortex shedding suppression and wake control. One effective method for controlling wake turbulence involves installing small airfoil sections at the trailing edge, which can significantly inhibit vortex shedding. Additionally, understanding the relationship between internal pressure pulsations and unstable vortices in hydraulic rotating machinery remains a critical challenge. Several scholars have proposed valuable insights into this correlation. Shu et al. (2021a, 2021b) utilized the Q-criterion to reveal the relationship between tip leakage vortices and pressure pulsation intensity in vane-type multiphase pumps. Zhao et al. (2021) employed numerical simulations to demonstrate a strong correlation between the development of trumpet-shaped vortices and pressure pulsation coefficients in axial-flow pumps. Feng et al. (2016) found that tip clearance vortices exacerbate pressure pulsation amplitudes from the hub to the shroud in axial-flow pumps.

In summary, while significant progress has been made in vortex research for hydraulic machinery, investigations specifically targeting the destabilization mechanisms of vortices in vane-type multiphase pumps remain notably scarce. This study addresses this critical gap by systematically examining strong-weak vortex evolution through an integrated theoretical framework combining vorticity decomposition, secondary flow diagnosis, and rigid vorticity vector analysis. The research uniquely reveals the "front-middle-rear leakage vortex" structural concept and establishes the correlation between blade geometry and vortex evolution patterns. Furthermore, it quantitatively demonstrates how gas accumulation and flow conditions govern vortex transitions and pressure pulsation characteristics. These findings provide both theoretical foundations for understanding vortex-pulsation interactions and practical insights for optimizing multiphase pump stability under complex gas-liquid transport conditions, representing an advancement in managing unstable flows in multiphase pumping systems.

2. Theoretical foundation

2.1. Governing equations

In numerical simulations of flow fields within hydraulic rotating machinery, although the fluid motion state is complex, it still adheres to three fundamental conservation laws: the continuity equation, momentum conservation, and energy conservation. For this study, which does not consider heat transfer or liquid-phase compressibility, the primary governing equations employed are the continuity equation and momentum equation, expressed as Eqs. (1) and (2) respectively.

$$\frac{\partial}{\partial t}(\rho) + \nabla \cdot (\rho V) = 0 \tag{1}$$

$$\frac{\partial}{\partial t}(u_i) + \frac{\partial}{\partial t}\left(u_i u_j\right) = -\frac{1}{\rho}\frac{\partial P}{\partial x_i} + f_i + \frac{1}{\rho}\frac{\partial}{\partial x_j}\left(\mu \frac{\partial u_i}{\partial x_j}\right) \tag{2}$$

here, ρ is the density of the medium, P denotes the pressure, t represents time, V indicates the velocity vector, u_i, u_j (where the subscripts i and j take values of 1, 2, 3) correspond to the velocity components in the x, y, and z directions, f_i stands for the body force term, and μ is the dynamic viscosity.

2.2. Turbulence model

In actual operation of the vane-type multiphase pump, the two-phase flow exhibits complex turbulent motion, making the selection of an appropriate turbulence model crucial for studying internal flow characteristics. In engineering numerical simulations, the primary methods include direct numerical simulation (DNS), Reynolds-averaged Navier Stokes (RANS), and LES. While DNS and LES demand high computational resources and extended simulation times, the RANS model offers lower computational requirements while adequately capturing turbulent flow behavior. This study adopts the SST k-ω turbulence model, which excels in simulating wall shear stress and secondary flows near boundaries while maintaining computational efficiency.

2.3. Multiphase flow model

The working medium in this study is gas-liquid two-phase flow. In recent years, the selection of multiphase flow models has predominantly focused on homogeneous and heterogeneous approaches. Homogeneous model assumes identical velocity and pressure fields for both phases in flow field calculations, implying no interphase velocity slip or pressure gradients. Heterogeneous model allows independent velocity and pressure fields with explicit consideration of interphase forces, requiring coupled two-phase momentum equations. While the homogeneous model offers advantages in computational efficiency (faster convergence and lower resource demands), the heterogeneous model achieves higher accuracy by resolving phase interactions and interfacial dynamics, albeit at increased computational cost. To ensure fidelity in simulating gas-liquid interfacial phenomena, this study adopts the heterogeneous model. Its capability to capture phase separation and momentum exchange aligns with the complex flow patterns observed in vane-type multiphase pumps.

2.4. Potential rothalpy theory

Wang et al. (2021a, 2021b) proposed a rigid vorticity transport equation as a new theoretical tool for analyzing and describing the evolution of vortical structures in hydro-energy machinery and a general alternate loading technique, which aims to control the potential rothalpy theory by adjusting the blade loading distribution, thereby effectively suppressing typical secondary flows.

The vorticity decomposition theory separates vorticity into rotational vorticity and deformational vorticity. From an engineering application perspective—particularly concerning vortex stall characteristics—the potential rothalpy approach, as a secondary flow diagnostic theory, can effectively quantify vortices and other secondary flows, thereby uncovering the underlying causes of unstable flow patterns. In the pressure-boosting unit of a vane-type multiphase pump, when fluid flows parallel to the blade profile (i.e., the fluid's trajectory aligns with the blade's geometric contour), the impeller blades operate with high efficiency, and the total rothalpy I remains conserved along the streamline. The expression is as follows:

$$I = I_\mathrm{p} + I_\mathrm{k} \tag{3}$$

In Eq. (3): I_p represents the potential rothalpy, I_k denotes the kinetic rothalpy.

Here, since the kinetic rothalpy is always perpendicular to the relative velocity vector direction, it does not participate in flow modifications. Therefore, the potential rothalpy gradient (PRG) is considered the primary factor affecting fluid flow stability.

The expression for potential rothalpy is:

$$I_P = \frac{P}{\rho} - \frac{1}{2}\omega_\mathrm{i}^2 r^2 \tag{4}$$

In Eq. (4): r represents the radial coordinate, ω_i denotes the impeller angular velocity.

The PRG is expressed by Eq. (5), which quantifies the magnitude of the PRG within the flow passage and serves as a diagnostic metric for secondary flows. Taking the divergence of both sides of Eq. (5) yields the Poisson equation for the velocity field, given as Eq. (6).

$$V \cdot \nabla V = -\nabla I_\mathrm{p} 2\omega \cdot V \tag{5}$$

$$\Delta I_\mathrm{p} - 2\omega \cdot \nabla V = 2Q_\mathrm{r} \tag{6}$$

where Q_r represents the second invariant of the velocity gradient tensor vortex formation ∇V is considered to occur when the rigid vorticity significantly dominates the deformational vorticity, when the relative vortex intensity Ω_R in Liutex-Omega theory exceeds 0.5. Here, $Q_\mathrm{r} > 0$ is equivalent to $\Omega_\mathrm{R} > 0.5$, which further demonstrates that the magnitude of the PRG governs the generation of secondary vortices.

As a diagnostic function for flow stability assessment, the SI value can effectively quantify the intensity of secondary flows within the flow domain. Its expression is given by:

$$\mathrm{SI} = \frac{\mathrm{PRG}}{F_\mathrm{c}} = \frac{\| -\nabla I_\mathrm{p} \|_2}{\| -\omega \times V \|_2} \tag{7}$$

For vane-type multiphase pumps, when the geometric configuration of the blades is fixed, the flow demonstrates higher stability when the PRG is lower than the coriolis force F_c. The PRG arises from the interaction between the blades and the fluid. Identifying an appropriate PRG to balance the coriolis force F_c enables the fluid to maintain stable flow along the blade profile. Zhao et al. (2023) found that in axial-flow vane pumps, the flow becomes highly unstable when the SI exceeds 1.

The analysis based on rigid vorticity provides clearer characterization of the macroscopic generation mechanism of secondary flows within the impeller, which facilitates more definitive understanding of the intrinsic flow characteristics in the impeller passage.

2.5. Vector decomposition principle of rigid vorticity

The expression for rigid vorticity ω_R can be simplified as Eq. (8), λ_ci represents the imaginary part of the complex conjugate eigenvalues of the velocity gradient tensor, ω denotes the vorticity vector, r indicates the vortex axis direction.

$$\omega_\mathrm{R} = \left[\omega \cdot r - \sqrt{(\omega \cdot r)^2 - 4\lambda_\mathrm{ci}^2}\right] \cdot r \tag{8}$$

Assume the Cartesian coordinates (x, y, z) are rotated by an angle θ about the z-axis, resulting in new coordinates (x_ξ, y_ξ, z_ξ), the corresponding coordinate transformation is given by:

$$\begin{pmatrix} \cos\phi & -\sin\phi & 0 \\ -\sin\phi & -\cos\phi & 0 \\ 0 & 0 & 1 \end{pmatrix} \begin{bmatrix} x \\ y \\ z \end{bmatrix} = \begin{bmatrix} x_\xi \\ y_\xi \\ z_\xi \end{bmatrix} \tag{9}$$

Assume the rigid vorticity vector at a certain point in the fluid domain is (R_x, R_y, R_z). Taking the z-axis as the rotation axis, it can be decomposed in cylindrical coordinates as (R_c, R_r, R_z). The rigid vorticity components can thus be obtained as follows: circumferential component from Eq. (10), the radial component from in Eq. (11), the axial component from Eq. (12).

$$R_\mathrm{c} = R_y \sin\theta - R_x \cos\theta \tag{10}$$

$$R_\mathrm{r} = -R_x \sin\theta - R_y \cos\theta \tag{11}$$

$$R_\mathrm{c} = R_z \tag{12}$$

2.6. Pressure pulsation theory

To investigate the correlation between vortex flow and pressure pulsations in vane-type multiphase pumps, this study introduces calculations for both pressure pulsation amplitude and pressure pulsation intensity, represented by Eqs. (13) and (14), respectively.

$$C_\mathrm{p} = \frac{P_\mathrm{i} - \overline{P}}{0.5\rho U_\mathrm{tip}^2} \tag{13}$$

$$I_\mathrm{pf} = \frac{\sqrt{\frac{1}{N}\sum_{i=1}^{N}(P_\mathrm{i} - \overline{P})}}{0.5\rho U_\mathrm{tip}^2} \tag{14}$$

In the analysis of pressure characteristics, Eq. (13) defines the pressure coefficient C_p, where P_i represents the instantaneous pressure, $\overline{P}$ denotes the time-averaged pressure, ρ is the fluid density, and U_tip indicates the impeller inlet velocity. Eq. (14) quantifies the pressure pulsation intensity I_pf.

3. Numerical calculation method

3.1. Physical model and mesh generation

Fig. 1 shows the schematic diagram of the main flow components of a single-stage vane-type multiphase pump, including the impeller, guide vanes, pump casing, and inlet/outlet pipelines. Among these components, the pressure-boosting unit (impeller and guide vane) serves as the core of the vane-type multiphase pump. The design philosophy follows the "three-dimensional flow theory" of fluid machinery. The guide vane structure references compressor design principles, which helps break up gas bubble accumulation. The impeller blades feature a large wrap angle to increase the single-flow-passage area, while longer blades are more conducive to energy transfer to the fluid. Table 1 presents the structural parameters of the pressure-boosting unit in the studied vane-type multiphase pump.

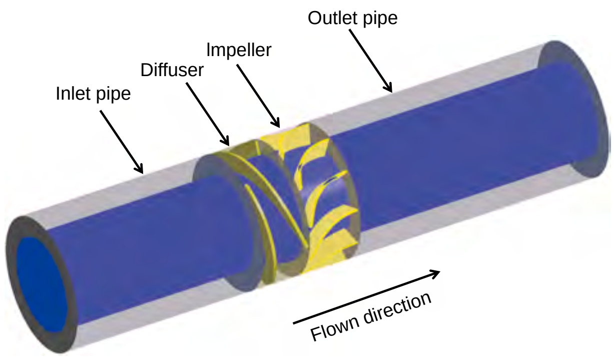

Fig. 1. Schematic diagram of flow passage in single-stage vane-type multiphase pump.

To enhance computational convergence and obtain high-quality mesh, structured meshes were adopted for all four fluid domains within the pump. Specialized mesh refinement was implemented at the 1.0 mm tip clearance region with 30 boundary-layer meshes to achieve high-resolution capture of TLV spatial distribution patterns and transient vortex evolution characteristics. The y^+ on the impeller and diffuser blade surface is 0–65 and 0–90, which meets the demand of the turbulence model and scalable wall function. Fig. 2 shows the computational domain mesh schematic of the pressure-boosting unit in the studied vane-type multiphase pump.

3.2. Boundary conditions and solver settings

This study involves both steady-state and transient numerical simulations of the single-stage pump operating at 3000 r/min. Air and water were selected as the gas-phase and liquid-phase media, with their phase states configured as dispersed and continuous, respectively. The SST k-ω turbulence model was applied to the liquid phase, while the dispersed phase zero-equation model was adopted for the gas phase. A heterogeneous flow model was chosen to characterize the interphase drag forces between the gas and liquid phases.

The impeller speed of the vane-type multiphase pump was set to 3000 r/min. Based on the inlet flow rate (100 m^3/h), the boundary conditions were configured as follows: velocity inlet at 2.689 m/s and pressure outlet at 7 atm. The walls of the pressure-boosting unit were set to no-slip conditions, with the rotor-stator interface employing a frozen rotor approach for steady-state simulations. To accelerate convergence and reduce computational time in transient simulations, the steady-state results were used as initial values, while the transient frozen rotor method was applied to the rotor-stator interface. Numerical convergence was determined by monitoring either the RMS residuals (set to 10^{-5}) or the stabilization of the inlet-outlet pressure difference.

Table 1
Design parameters of the pressure-boosting unit in vane-type multiphase pump.

Parameter	Impeller	Guide vane	Unit
Rim diameter	161	161	mm
Inlet hub diameter	113	126	mm
Outlet hub diameter	126	113	mm
Blade inlet angle	9°/6°	0	
Blade outlet angle	27°/24°	35°	
Axial length	60	66	mm
Number of blades	3	11	

3.3. Mesh independence verification

Table 2 presents the mesh independence verification scheme for the computational domain. The first mesh scheme serves as the baseline, while beyond the third mesh scheme, the relative hydraulic efficiency and relative head of the multiphase pump exhibit minimal variations. Therefore, considering both accuracy and computational economy, the third mesh scheme was adopted for the simulations. Table 2 shows the mesh independence verification under water conditions.

Fig. 3 displays the velocity streamline distribution and y^+ value distribution on the pressure-boosting unit walls. Shi and Wang (2019) and Shi et al., 2020b) demonstrated that for high-Reynolds-number conditions, the y^+ values for the SST model should remain below 100, whereas for low-Reynolds-number conditions, y^+ values should range between 1 and 9. As evident from Fig. 3, most regions on the impeller walls correspond to high-Reynolds-number zones, with only localized areas on the blade surfaces representing low-Reynolds-number regions. The corresponding y^+ values in these areas meet the specified requirements. In summary, the simulated y^+ values satisfy the SST model's criteria across different Reynolds number regimes.

Fig. 4 shows the monitoring points set in the flow passage of the pressure-boosting unit of the vane-type multiphase pump, aiming to measure pressure variations at these points and further verify the reliability of the simulation. To validate the unsteady calculation reliability, five points each were arranged in the impeller and guide vanes, designated as IP1~IP5 and DP1~DP5 respectively.

Fig. 5 presents the pressure variation at monitoring point DP3 over one rotation period, calculated using three time-steps (5.56×10^{-5}, 1.11×10^{-4}, and 1.67×10^{-4} s) corresponding to 1°, 2°, and 3° of impeller rotation respectively. The results demonstrate good agreement among all three time-steps, indicating excellent mesh stability in transient calculations with minimal sensitivity to time step variations. Considering computational resource allocation, the second time step (1.11×10^{-4} s) was selected for numerical analysis as the optimal choice. For transient calculations, the converged steady-state results served as initial conditions. To ensure accuracy, each operating condition's transient simulation duration was set at 0.46 s, with analysis conducted on the periodic evolution during the final revolutions.

4. Numerical calculation and experiment

4.1. Experimental system

Fig. 6 shows the physical components of the pressure-boosting unit in the multiphase pump, including the impeller, guide vanes, and pump casing. The impeller, manufactured from stainless steel, serves as the primary energy conversion component. The blade count, wrap angle, and inlet/outlet angles of both the guide vanes and impeller correspond to the specifications in Table 1, with a 1.0 mm clearance between the impeller blades and outer casing. To facilitate observation of flow patterns and their transient evolution within the impeller, the surrounding casing was constructed from transparent glass. The experimental investigation included multiple operational conditions, focusing on performance characteristic testing and flow pattern visualization. The flow visualization employed high-speed photography to capture flow dynamics in the impeller passages, using purified water and air as the two-phase media.

During the experimental process, the following procedures were primarily implemented: First, water from the tank and air from the gas reservoir were thoroughly mixed through pipelines and then delivered to the pressure-boosting unit. After stable

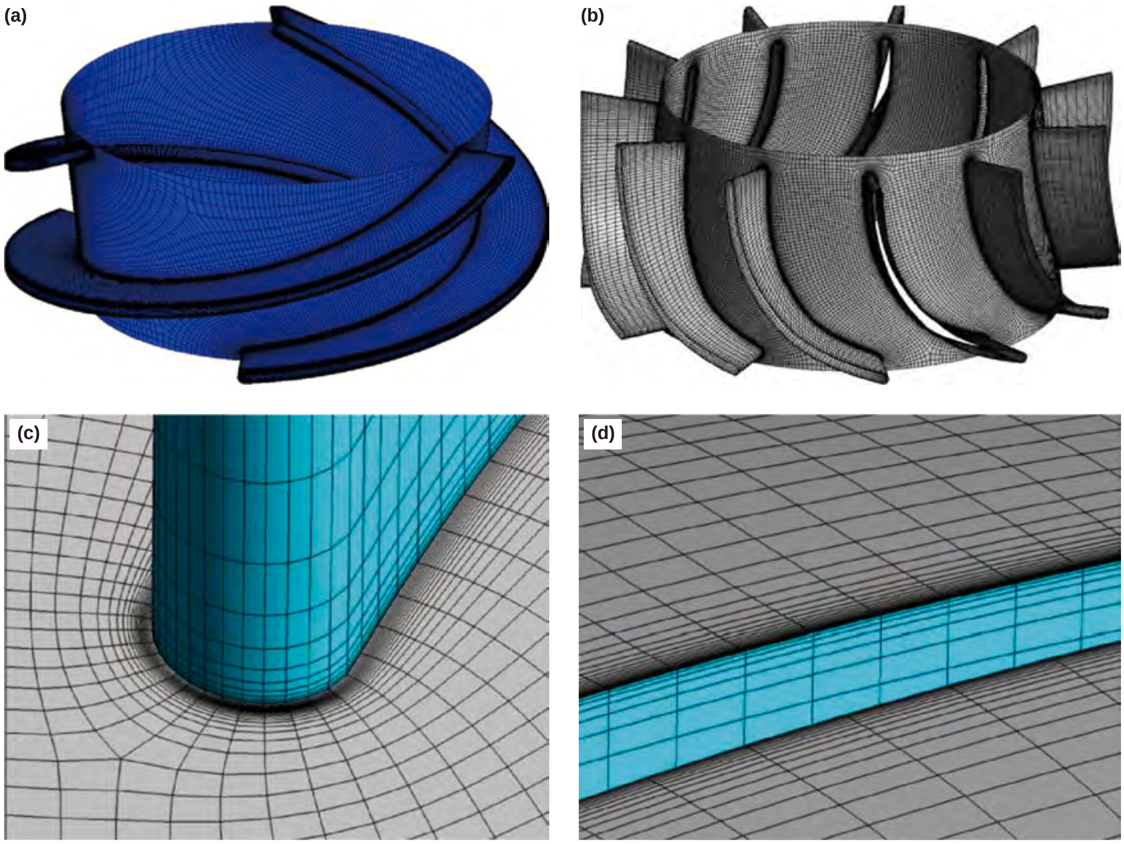

Fig. 2. Schematic of computational domain mesh: (**a**) Impeller mesh; (**b**) Guide vane mesh; (**c**) Hub-region mesh of impeller; (**d**) Magnified view of the blade surface boundary layer mesh refinement.

Table 2
The grid independence verification scheme for the computational domain.

Case	Number of meshes ($\times 10^4$)	Relative head	Relative efficiency
1	221	1.0	1.0
2	334	1.019	1.024
3	456	1.062	1.042
4	598	1.048	1.041

operation of the vane-type multiphase pump was achieved, experimental data including inlet/outlet pressure and torque were recorded using measurement instruments. Second, when operating under different flow rates or gas volume fraction conditions, adjustments were made by regulating the inlet opening or adjusting the air intake valve, followed by observation and recording of experimental data. Finally, high-speed cameras were employed to capture flow patterns within the passage. The equipment test bench for the vane-type multiphase pump is shown in Fig. 7.

4.2. Comparison between numerical and experimental results

Fig. 7 shows a photograph of the self-built multiphase-pump test platform. This consists of four main parts: the gas transmission system, infusion system, gas–liquid mixing system, and multiphase pump test system. Fig. 8 shows a schematic diagram of this experimental system. To facilitate visualization of the internal flow of the multiphase pump, the shell material of the booster unit was made from transparent polymethylmethacrylate. Under working conditions of 3000 rpm with pure water (flow rate 60–120 m^3/h) and gas–liquid two-phase condition (GVF = 5%), external-feature tests were conducted on a pump with tip clearance of 1.0 mm. Figs. 9 and 10 show characteristic curves summarizing the test outcomes along with the numerical calculation results. The errors in the head, efficiency, and output power between the test results and the calculations are all less than 5%. Due to the complex energy loss in the work of the multiphase pump, the numerical calculations can only predict part of the loss, so the values produced by the numerical calculations are greater than those measured in the tests, and this systematic error is unavoidable. In short, the numerical-calculation approach chosen herein was demonstrated to be reliable.

5. Results and analysis

5.1. Characteristics of TLV structures

Fig. 11 shows the distribution of tip leakage vortices in a single flow passage of the vane-type multiphase pump (IGVF = 10%). The leakage vortices are observed to extend from the suction side of the blade leading edge to the mid-region of the adjacent blade pressure side, primarily concentrated near the shroud. Three distinct leakage vortex types are identified: front leakage vortex, located near the passage inlet; main leakage vortex, found at the leading edge (LE) of the adjacent blade pressure side; rear leakage vortex, formed in the mid-region of the pressure side. Fig. 10 reveals two instability zones (Regions A and B) at the leading edge of Blade 2: region A, shows vortex filament breakage tendencies; region B, exhibits clear vortex shedding phenomena. The vortex stability progressively decreases from the main to rear leakage vortex, with the vortex core enlarging

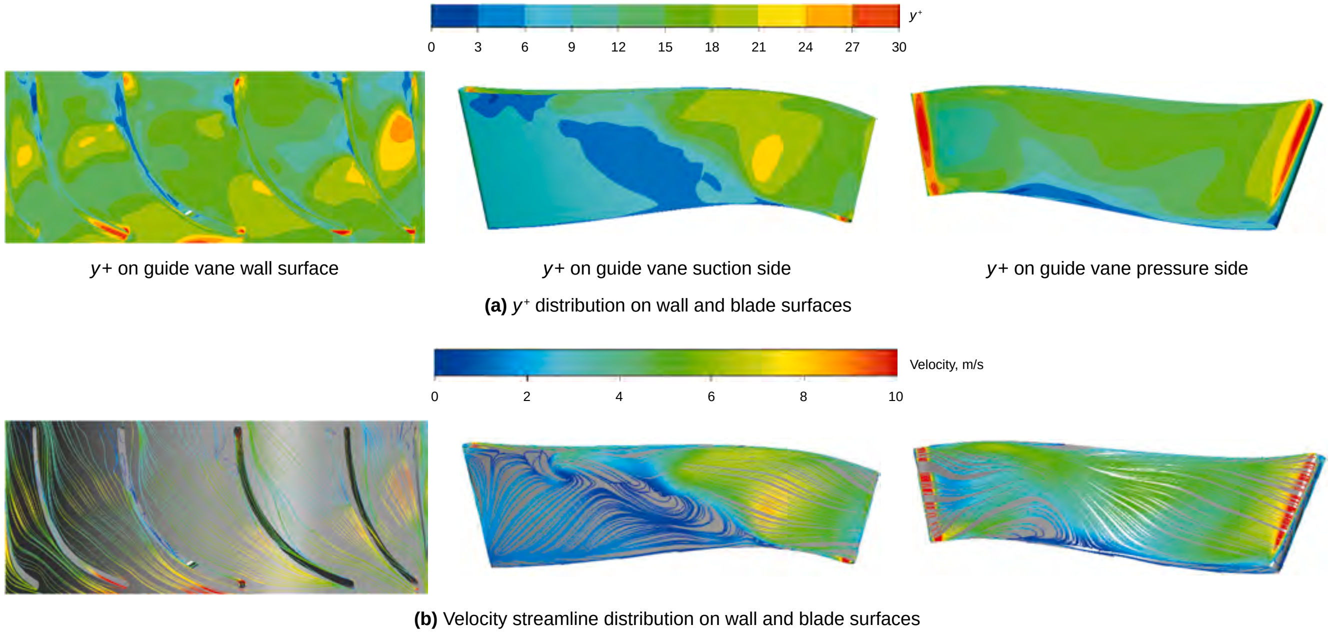

Fig. 3. Velocity streamline distribution and y^+ value distribution on the pressure-boosting unit walls.

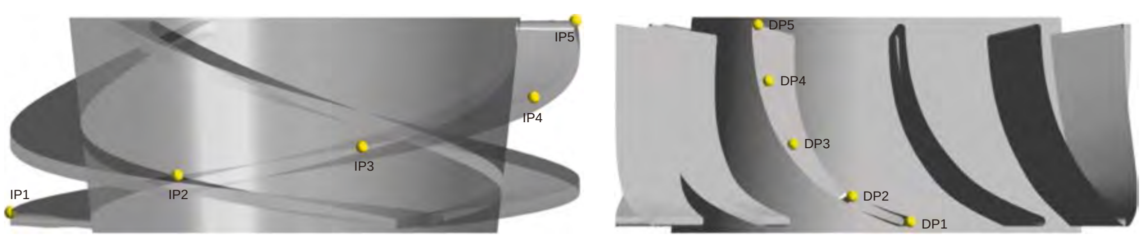

Fig. 4. Monitoring point distribution in impeller and guide vanes.

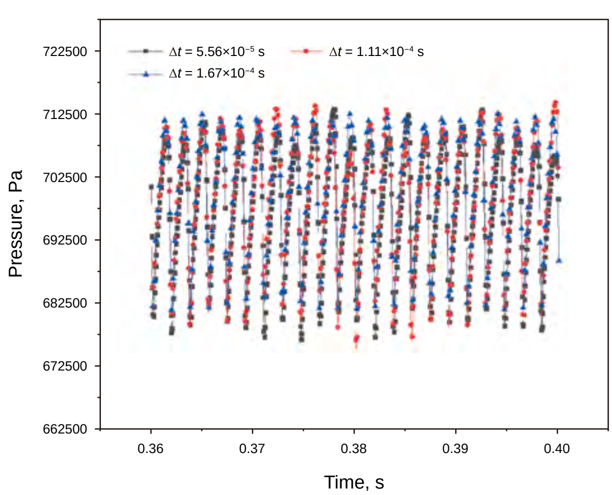

Fig. 5. Time step independence verification.

and eventually dissipating at the pressure side mid-region. Experimental visualization in Fig. 12 confirms the presence of vortex breakage zones in the impeller passage, with the shedding region matching Region A in Fig. 11.

This analysis indicates two inherent instability zones in the leakage vortex development. The spiral blade geometry is hypothesized as the primary contributor to this unique vortex distribution pattern. To investigate the instability mechanisms, the following section provides preliminary analysis of the vortex formation process.

Fig. 13 shows a schematic of the TLV evolution process from formation to diffusion, featuring simplified 2D-to-3D vortex modeling. In rotating machinery flow passages, vortex formation is fundamentally influenced by circumferential and axial velocity components or more precisely, its morphology is intrinsically linked to these directional velocities. Within the impeller passage of the vane-type multiphase pump, the TLV emerges through the combined action of axial and circumferential velocities. The rotational effect of the impeller further drives circumferential velocity to promote vortex diffusion throughout the passage, ultimately forming the elongated TLV structure. This supports the hypothesis that circumferential velocity plays a dominant role in both the formation and diffusion of leakage vortices.

To validate the aforementioned hypothesis, this study numerically partitions the rigid vorticity based on vorticity decomposition theory. Computational results reveal that the vortex core region exhibits high rigid vorticity concentration, termed as Strong Vortex Flow (SVF), while the peripheral vortex region with lower vorticity magnitudes is classified as Weak Vortex Flow (WVF). The classification between SVF and WVF is achieved through threshold selection of rigid vorticity isosurfaces. It should be noted that this threshold-based demarcation is not absolute but serves primarily for vortex component categorization. This section aims to uncover

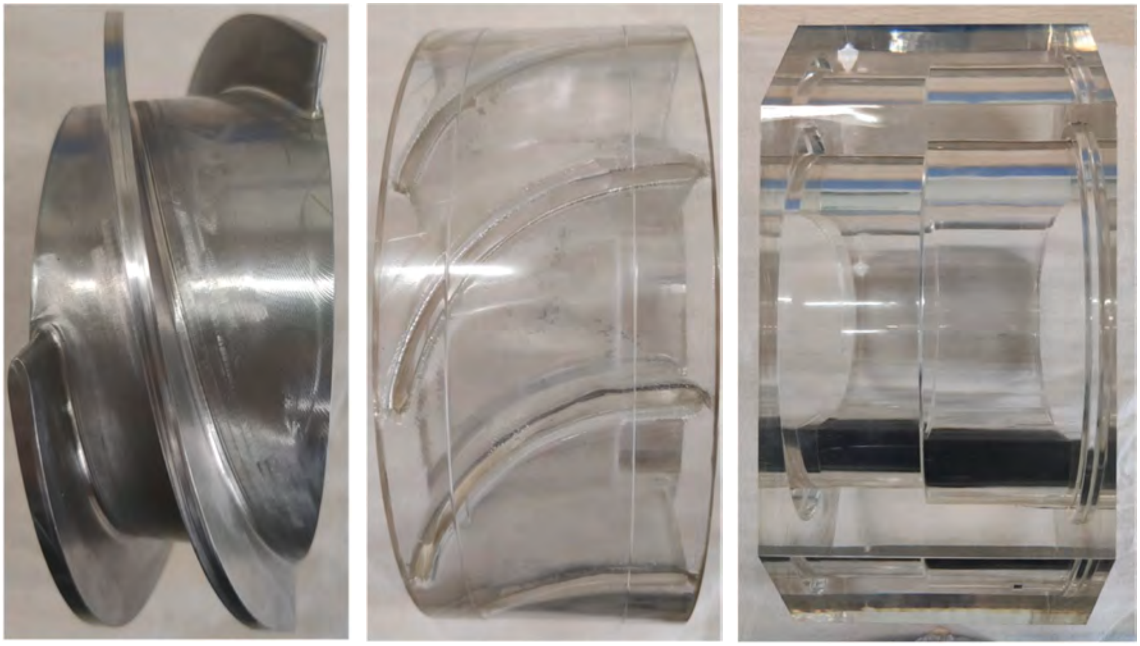

(a) Impeller **(b)** Guide vane **(c)** Pump casing

Fig. 6. The physical components of the pressure-boosting unit in the multiphase pump.

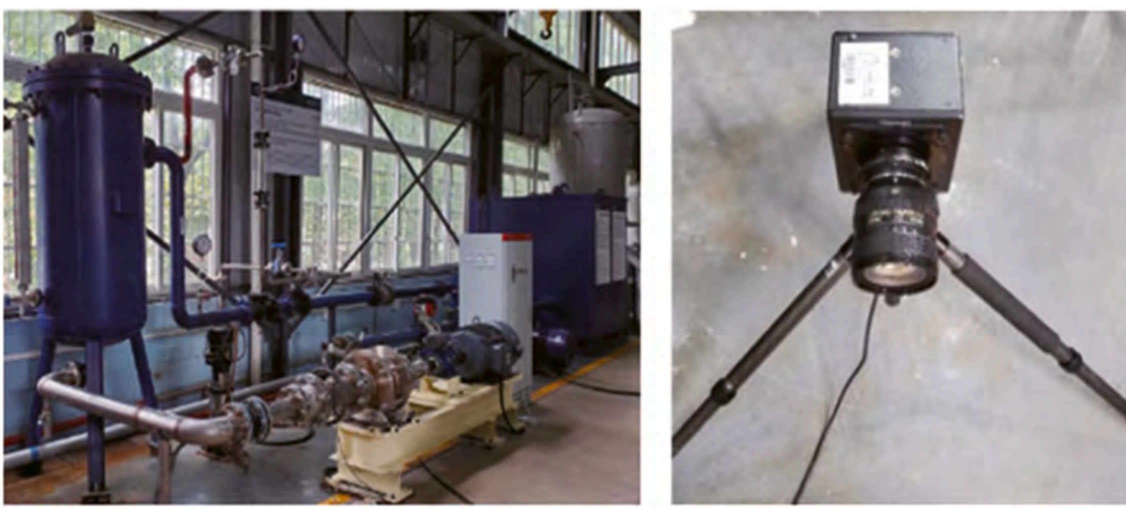

Fig. 7. Experimental test system (left) and high-speed camera setup (right).

the underlying mechanisms of leakage vortex "instability-fragmentation-shedding" through SVF/WVF analysis.

Fig. 13 shows the vortex distribution in the vane-type multiphase pump under pure water conditions, including SVF, Middle Vortex Flow (MVF), and WVF. To facilitate the investigation of leakage vortex trajectories, ten vortex core points (P_1–P_{10}) were extracted along the vortex axis. As shown in Fig. 14, the front and main leakage vortices primarily consist of SVF, whereas the rear leakage vortex is mainly composed of WVF.

In the pump flow passage, a low peak of rigid vorticity appears at the junction between the front and main leakage vortices. Theoretically, this region is prone to vortex dissipation and is therefore identified as the first breakage point of the leakage vortex. In the rear leakage vortex region, significant vortex shedding is observed, with the presence of gas phase notably amplifying the shedding scale. Consequently, the leakage vortex exhibits two primary dissipation zones, both predominantly consisting of WVF.

To further reveal the intrinsic causes of flow instability in the vane-type multiphase pump, a direct comparison was made between the circumferential velocity and vortex distribution at vortex core points. Fig. 15 shows the circumferential velocity distribution of leakage vortices and vortex cores under pure water conditions.

From Fig. 15(a), it is observed that from P_1 to P_5, as the SVF decreases, the circumferential velocity along the vortex axis gradually declines, particularly reaching a low peak at point P_5. This region primarily consists of WVF and corresponds to the first instability zone of the leakage vortex. A similar trend is observed in the P_5–P_{10} range, where the circumferential velocity at vortex core

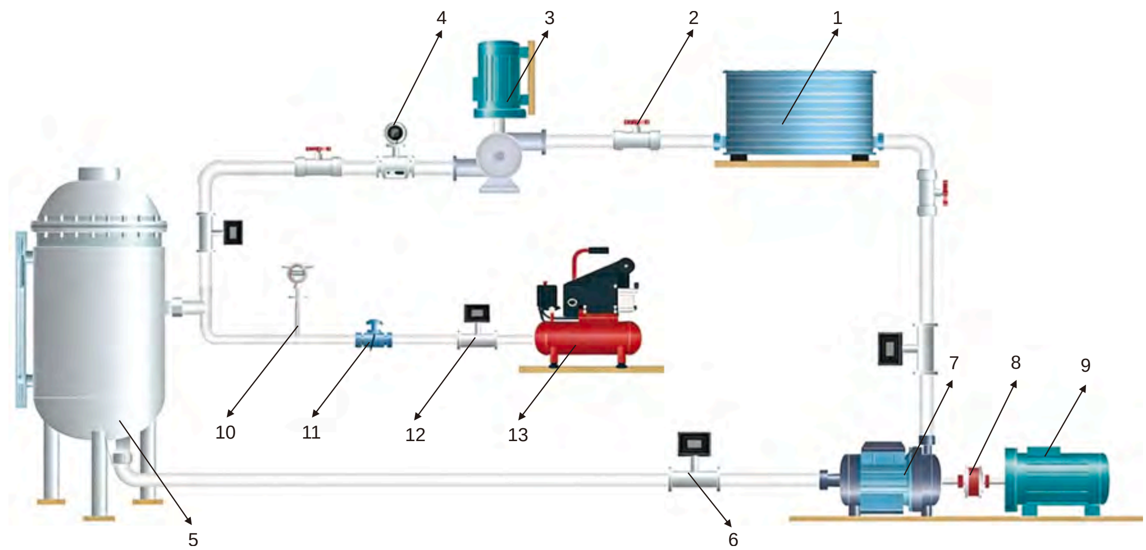

Fig. 8. Schematic diagram of the experimental system for the multiphase pump. 1: Water tank; 2: regulating valve; 3: booster pump; 4: flow meter; 5: gas–liquid mixing tank; 6: pressure sensor; 7: multiphase pump; 8: torque meter; 9: electric machine; 10: gas flow meter; 11: regulating valve; 12: gas pressure meter; 13: air compressor.

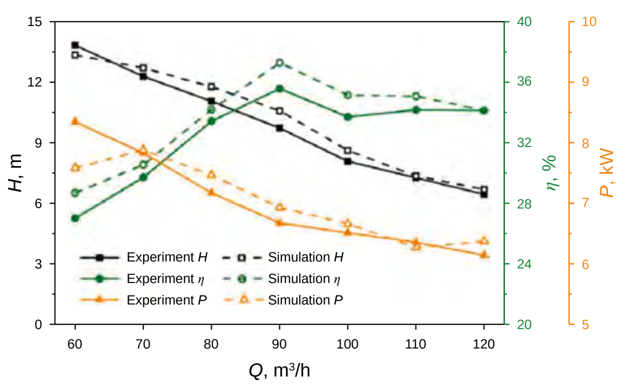

Fig. 9. Comparison of the results of tests and numerical simulations.

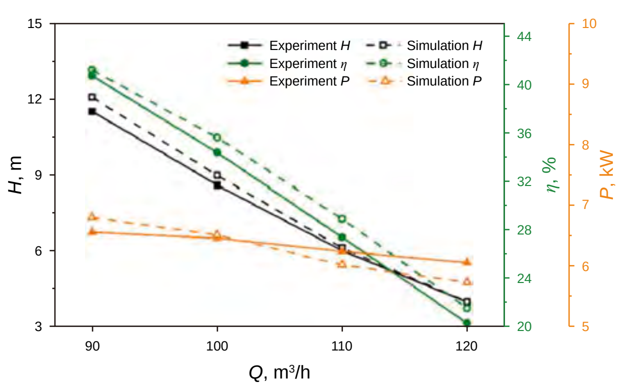

Fig. 10. Comparison of experimental and numerical simulation under gas–liquid two-phase conditions.

points exhibits a positive correlation with the SVF magnitude. Fig. 15(b) reveals that the MVF significantly increases in the front and main leakage vortex regions. The presence of the gas phase reduces the circumferential velocity along the vortex axis, and this localized decrease in circumferential velocity promotes stable vortex growth—especially the noticeable expansion of WVF scales.

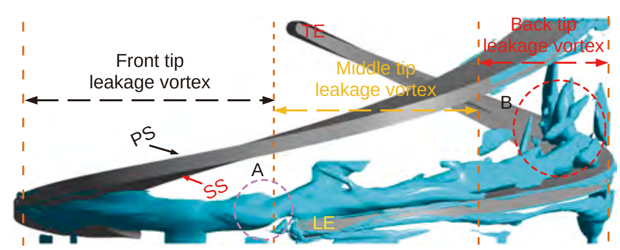

Fig. 11. Distribution of TLV (IGVF = 10%).

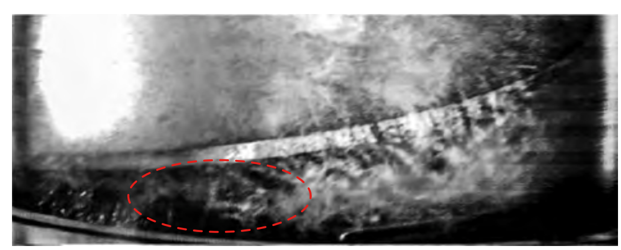

Fig. 12. Vortex breakage region (experimental visualization).

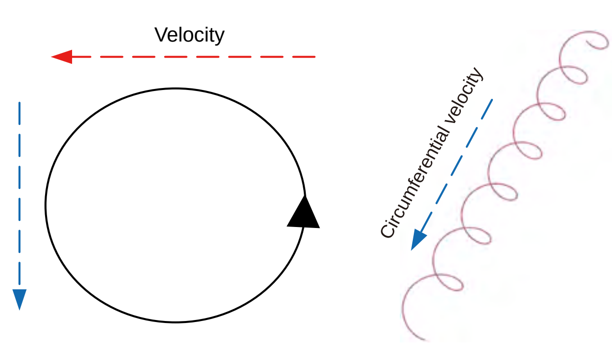

Fig. 13. Diffusion effects of TLV.

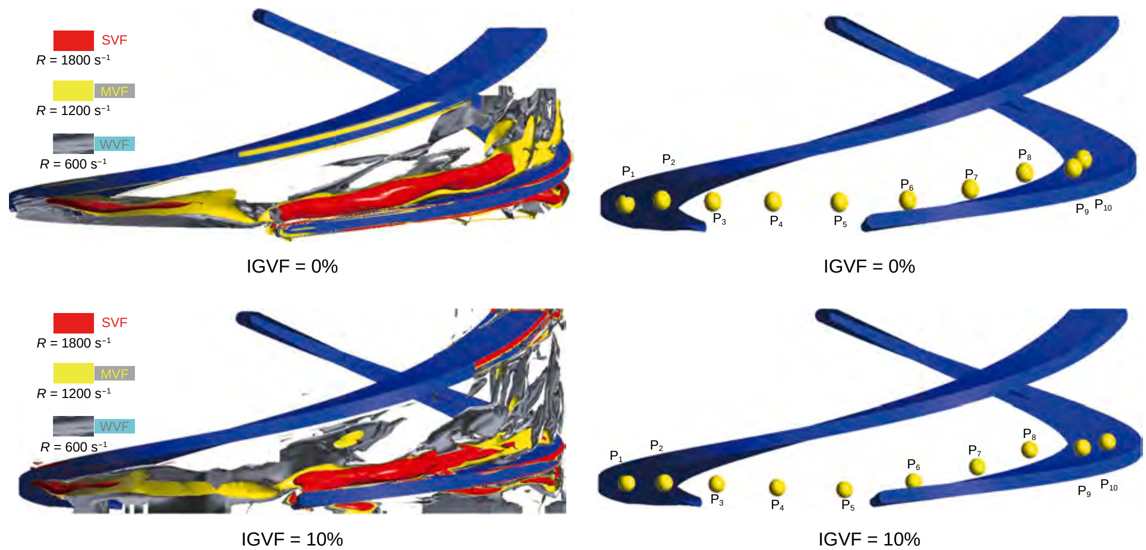

Fig. 14. TLV and vortex core trajectory distribution.

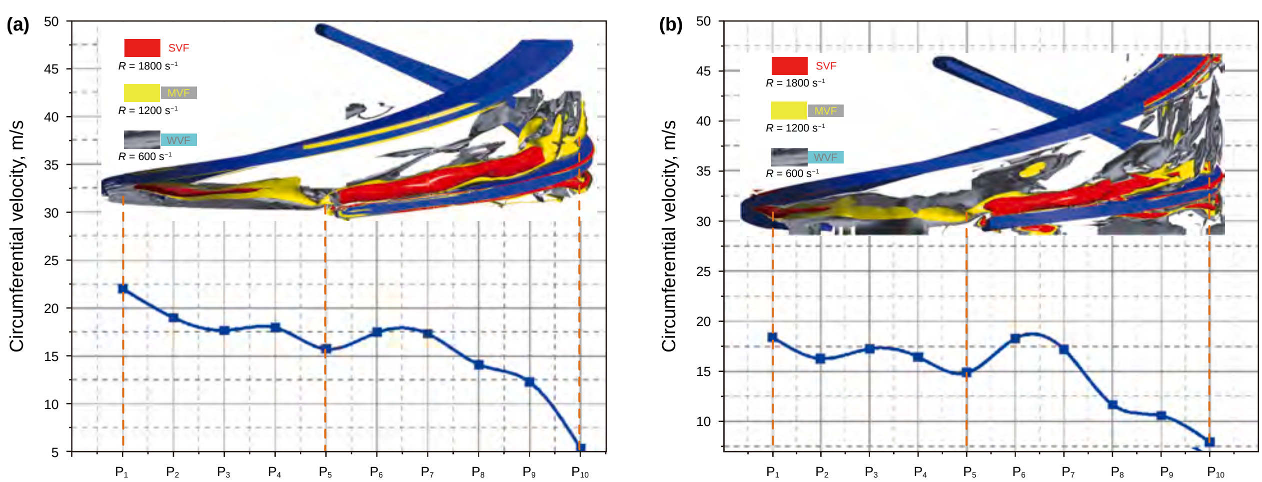

Fig. 15. Correlation between TLV and circumferential velocity distribution: (**a**) IGVF = 0%, (**b**) IGVF = 10%.

The gas phase further enlarges the vortex scales in the instability zones near P_5 and P_{10}.

These findings demonstrate that in the main leakage vortex region, the reduction in circumferential velocity along the flow direction leads to gradual vortex destabilization. As the circumferential velocity decreases, the leakage vortex continuously expands and diffuses, with SVF progressively transforming into MVF and WVF. Ultimately, vortex shedding occurs in the rear section of the flow passage. The gas phase facilitates the conversion of more SVF into WVF, thereby increasing the overall vortex scale within the flow passage.

Taking the IGVF = 10% condition as an example, this section focuses on analyzing the transient evolution process of leakage vortices within the flow passage. Fig. 16 illustrates the spatiotemporal evolution of TLV in the multiphase pump flow passage at 10% gas volume fraction.

From Fig. 16, it can be observed that during [T_0+ 1/20T, T_0+ 4/20T], as the SVF of the front leakage vortex gradually diffuses circumferentially and the SVF of the main leakage vortex diffuses in the opposite circumferential direction, the strong vortex flow (SVF) regions in both areas progressively expand. This significantly enhances their ability to entrain surrounding fluid, marking this phase as the growth stage for both the front and main leakage vortices. Simultaneously, the SVF of the front leakage vortex and the SVF of the main leakage vortex converge and compress toward each other. At $T_0 + 4/20T$, the leakage vortex undergoes strong vortex-induced torsion, leading to instability in this region and resulting in vortex breakage.

During [T_0+ 4/20T, T_0+ 6/20T], the SVF of the main leakage vortex gradually transforms into MVF (Middle Vortex Flow). By T_0+7/20T, the front leakage vortex dissipates into thin filamentary structures. In the phase [T_0+ 5/20T, T_0+ 8/20T], both MVF and SVF in the main leakage vortex successively diminish, completely dissipating by T_0+ 8/20T.

Additionally, from [T_0+ 1/20T, T_0+ 8/20T], vortex shedding in the rear leakage vortex gradually decreases, primarily due to the rapid reduction of SVF during the transition from the main to the rear leakage vortex. Theoretically, weak vortex flow (WVF) should destabilize first. However, before WVF can fully dissipate, SVF has already converted into WVF, leading to an observed phenomenon: within a specific time frame, the intensity of the leakage vortex decreases while its spatial scale progressively enlarges.

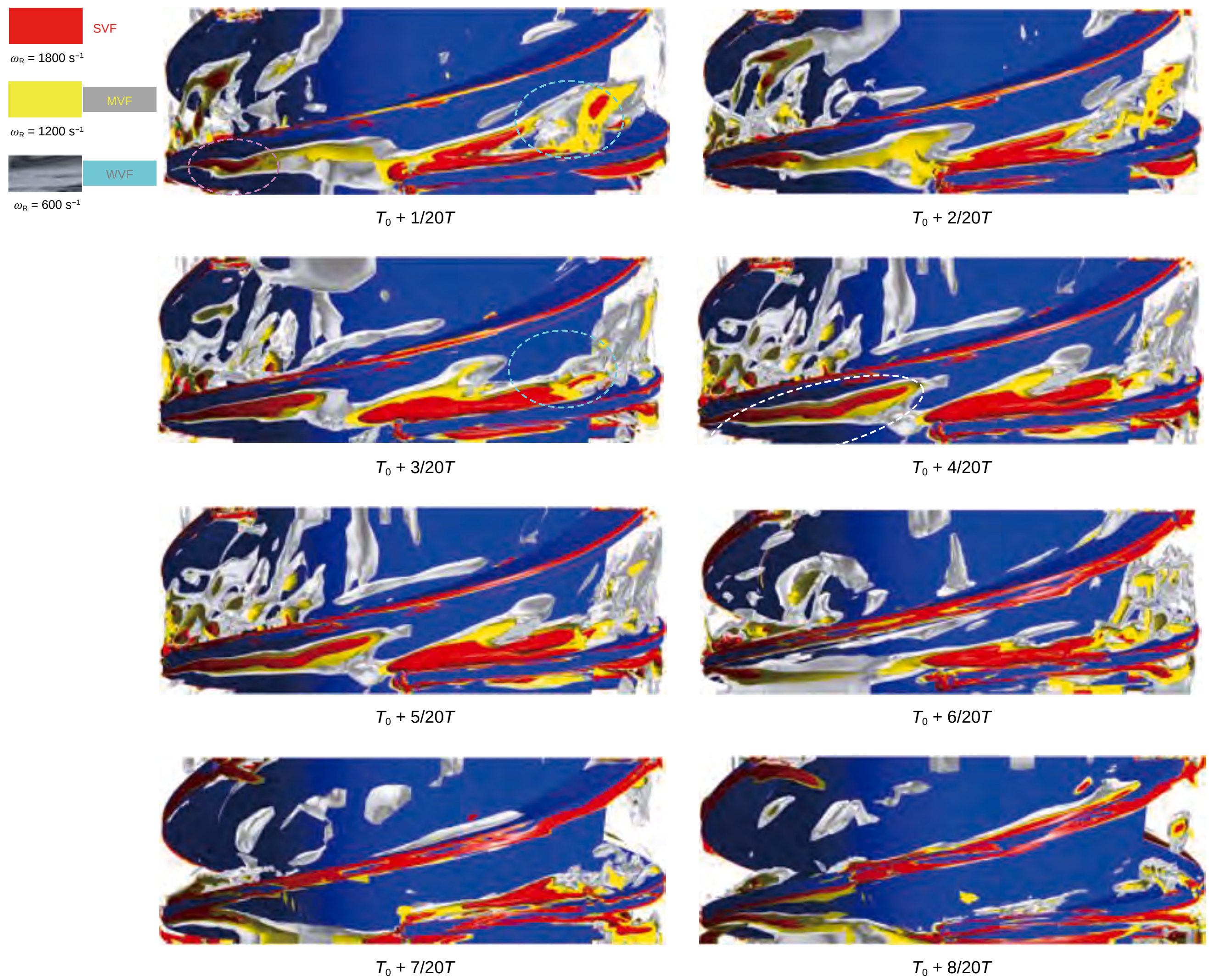

Fig. 16. Unsteady evolution of TLV under gas-liquid two-phase conditions (IGVF = 10%).

Fig. 17 presents high-speed photographic sequences of TLV evolution at 10% gas volume fraction. The images demonstrate that during [T_1, T_3], the front leakage vortex progressively diffuses while the main leakage vortex region expands, with their interfacial zone gradually developing instability that ultimately causes vortex breakage. Particularly at T_4, the breakage region becomes distinctly visible, and by T_6, the marked TLV area exhibits an extensive fracture zone.

5.2. Secondary flow mechanisms in vane-type multiphase pumps

Fig. 18 shows the PRG distribution on the blade surfaces of the vane-type multiphase pump. According to the governing equations, the PRG serves as the primary driver of relative motion within the impeller. Under ideal conditions, the potential rothalpy (I_p) contours should align with the streamlines ($V_r \times d_s = 0$). When the I_p contours closely follow the blade geometry, secondary flows are less likely to develop in the flow passage.

From Fig. 18, it is evident that the PRG on the blade suction side is significantly lower than that on the pressure side. Additionally, the I_p contours on the suction side exhibit better conformity with the blade profile, which explains the rapid increase in vortex intensity of the main leakage vortex downstream of the breakage point on the pressure side. Meanwhile, the I_p contours deviate more noticeably from the blade geometry near the leading and trailing edges, indicating that parameters such as blade angle and profile significantly influence fluid flow.

This section examines the potential rothalpy distribution on the suction and pressure sides at 10% gas volume fraction. Fig. 18(b) and (d) reveal that Part (1) and Part (2) are regions where secondary flow occurs. Near the trailing edge, the I_p contours show a distinct angular deviation from the blade shape, resulting in a high PRG that readily induces secondary flows. Fig. 18(e) and (f) provide magnified views of Part (1) and Part (2), respectively. On the suction side trailing edge, the mismatch between the blade angle and streamlines leads to a sharp increase in the potential rothalpy gradient, causing flow disturbances and the formation of multiple vortices. In contrast, the I_p contours on the pressure side trailing edge align more closely with the blade profile, resulting in fewer vortices in this region.

Therefore, blade profile design profoundly impacts flow stability. Establishing a correlation between blade geometry and secondary flows, such as leakage vortices, is crucial for effective flow control.

Fig. 19 identifies the front, main, and rear leakage vortex regions as primary instability zones, where the I_p contours on both

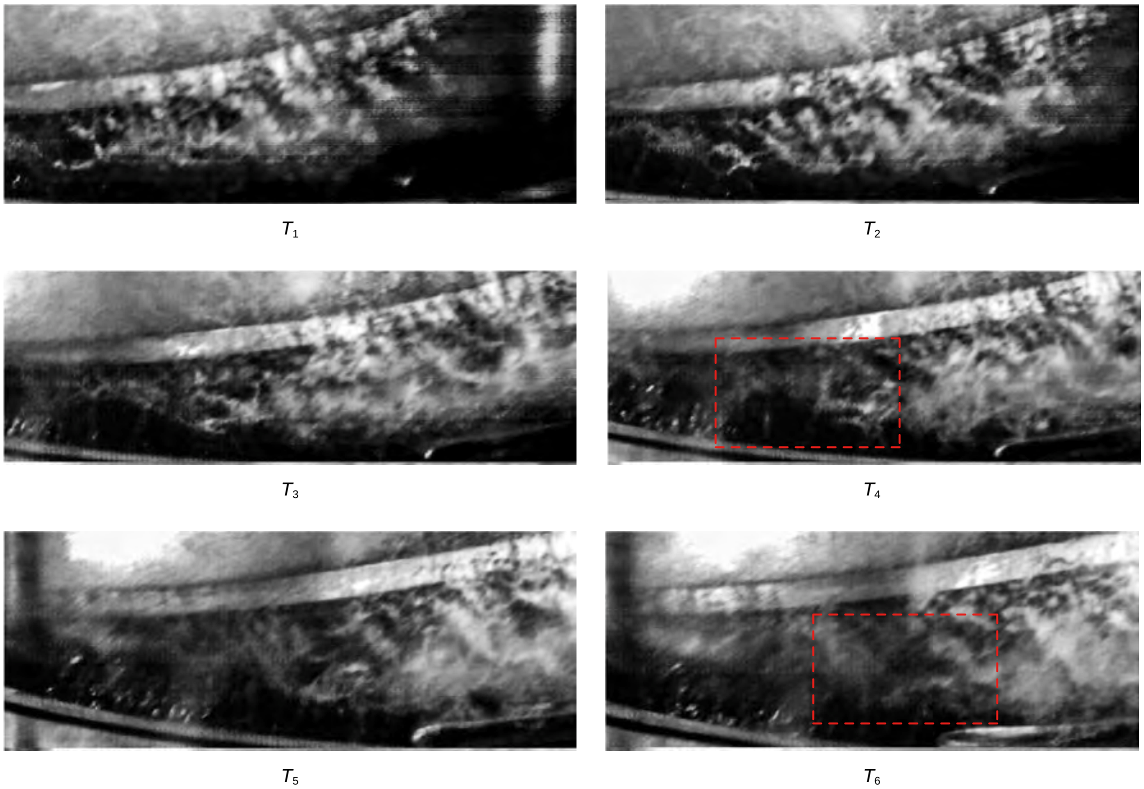

Fig. 17. High-speed photographic sequence of TLV breakage region evolution (IGVF = 10%).

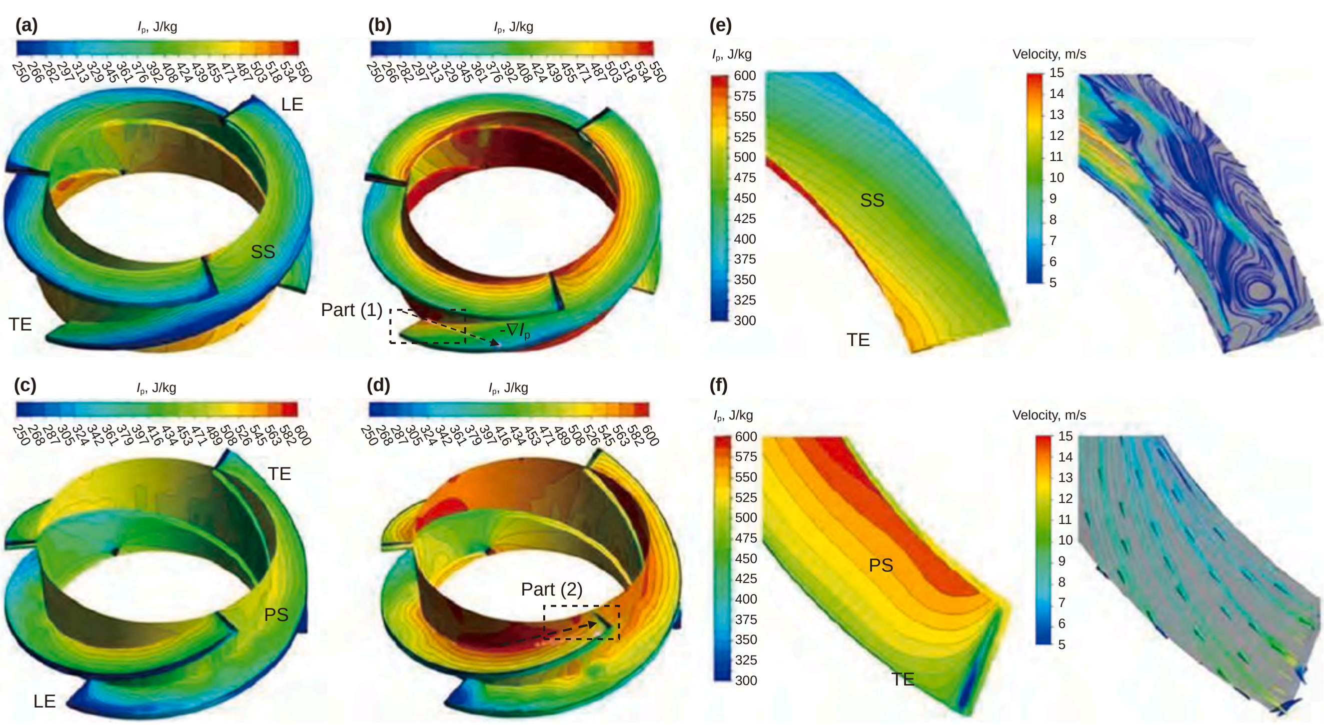

Fig. 18. PRG distribution on impeller blade surfaces: (**a**) Pressure surface (PS), IGVF = 0%; (**b**) Pressure surface, IGVF = 10%; (**c**) Suction surface (SS), IGVF = 10%; (**d**) Suction surface, IGVF = 10%; (**e**) Enlarge of Part (1); (**f**) Enlarge of Part (2).

suction and pressure sides significantly deviate from the blade profile—a key factor in vortex destabilization. Fig. 19(a) and (b) show that the initiation point of the front leakage vortex coincides with the suction-side leading edge, aligning precisely with the onset of I_p contour deviation and a locally high potential rothalpy gradient. Elsewhere along the leading edge, well-distributed I_p

contours correlate with minimal vortex activity, demonstrating effective flow control through blade profile design.

Fig. 19(c) and (d) reveal severe I_p contour distortion near the pressure side, spatially coinciding with the main leakage vortex. As the tip-region I_p contours progressively deviate from the blade geometry, the leakage vortex forms and diffuses into the passage. Conversely, when I_p contours realign parallel to the blade profile in the rear section, the vortex dissipates into fine-scale turbulent structures.

Fig. 20 displays the transient evolution of leakage vortices and SI values (ratio of PRG to Coriolis force, directly indicating flow stability) under pure water conditions. The SI distribution on blade surfaces synchronizes with vortex spatiotemporal evolution. During 0.414–0.42 s (vortex growth phase), the main leakage vortex expands while adjacent blades exhibit rising SI values, both propagating toward the outlet. By $T = 0.42$ s, the rear leakage vortex evolves into a spiral pattern in the passage rear section. Under gas-liquid conditions, the leading-edge suction side shows intensified leakage vortices and SI values. Gas phase enlarges inlet instability zones, amplifies vortex scales, and accelerates diffusion—evidenced by prominent vortex shedding at $T = 0.42$ s. Despite gas-induced secondary flow enhancement, the blade rear section maintains stable SI values, proving that the long-wrap-angle helical blades effectively adapt to multiphase flows by suppressing vortex diffusion at design conditions.

5.3. Influence of gas volume fraction on flow characteristics and hydraulic performance

Fig. 21 presents the average distributions of turbulent dissipation rate, potential rothalpy gradient, and pressure boost values across the pump's inlet/outlet under varying gas volume fractions (IGVF). The data reveal that as IGVF increases from 0% to 20%, turbulent dissipation rate surges from 2332 to 7965 m^2/s^3, pressure boost declines from 80,640 to 56,135 Pa. A sharp rise in PRG occurs beyond 10% IGVF, accompanied by rapid deterioration of pressure-boosting performance. The most pronounced changes in turbulent dissipation, potential rothalpy gradient, and pressure differential emerge during the 15%–20% IGVF transition. These trends demonstrate that rising gas content intensifies flow instability, elevating turbulent dissipation and energy losses while degrading pressure-boosting capacity.

Fig. 22 shows the distribution of SI values at the impeller and guide vane outlets under different flow rates at IGVF = 10%. It can be observed from Fig. 22 that as the flow rate increases from 0.6*Q* to 1.0*Q*, the SI value at the impeller outlet of the vane-type multiphase pump decreases from 0.98 to 0.58, indicating a gradual reduction in overall secondary flow within the passage. At the low flow rate of 0.6*Q*, the average SI value at the impeller outlet approaches 1, suggesting poor flow uniformity under extreme operating conditions, which readily induces unstable vortices such

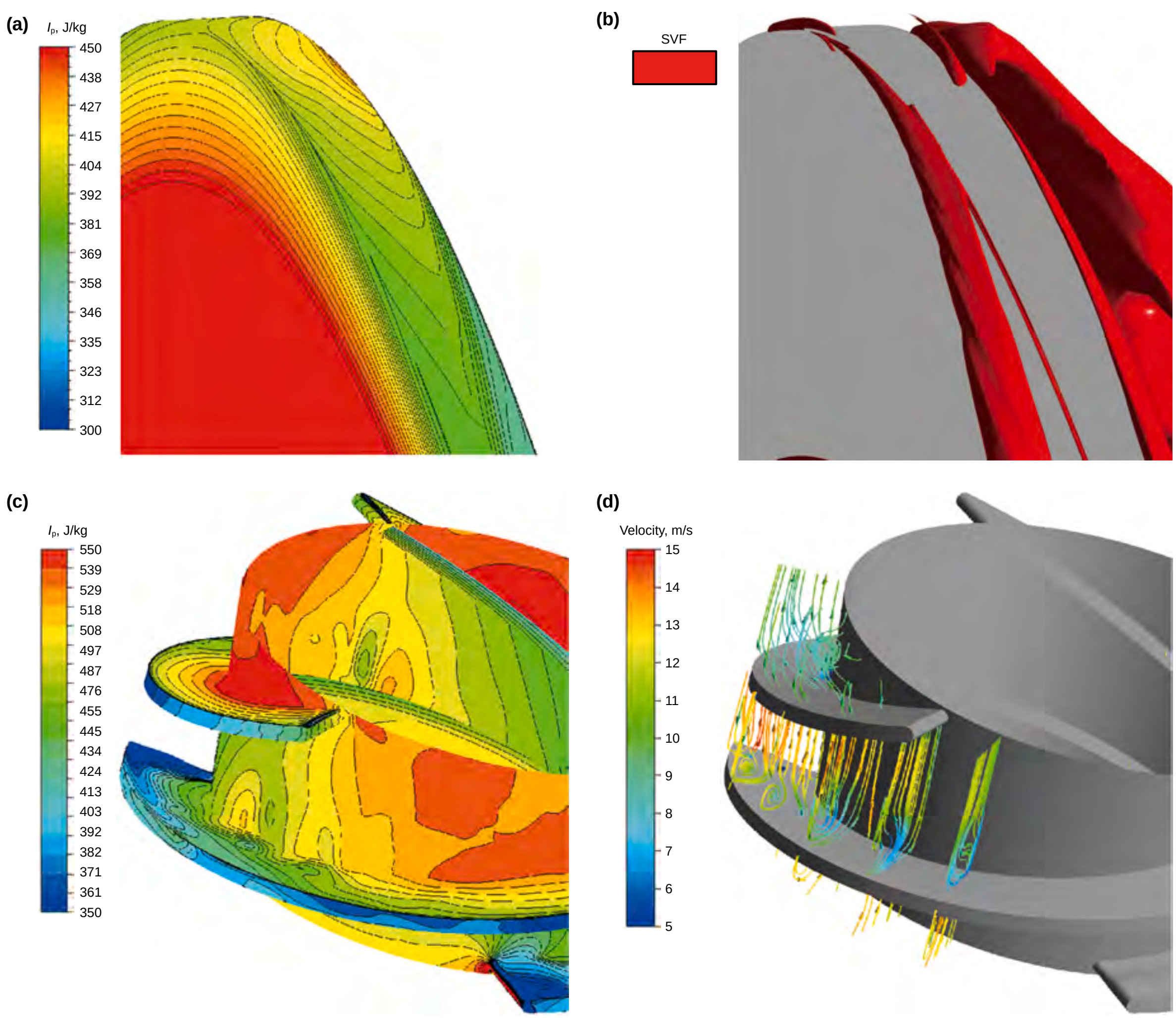

Fig. 19. TLV and PRG characteristic distributions (IGVF = 10%): (**a**) Distribution of the I_p; (**b**) F-TLV; (**c**) Distribution of the I_p; (**d**) Streamline of the M-TLV and the B-TLV.

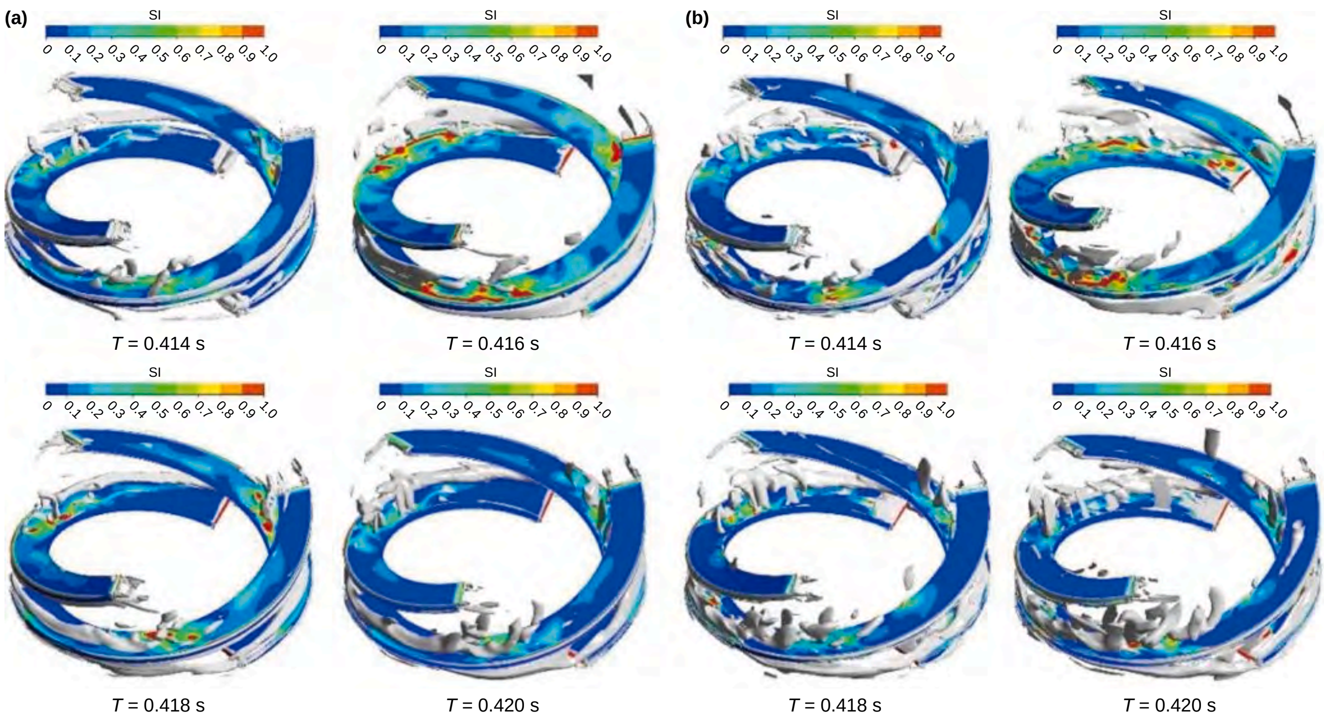

Fig. 20. Transient evolution of leakage vortex and stability index (SI) under two-phase conditions: (**a**) Pure water; (**b**) IGVF = 10%.

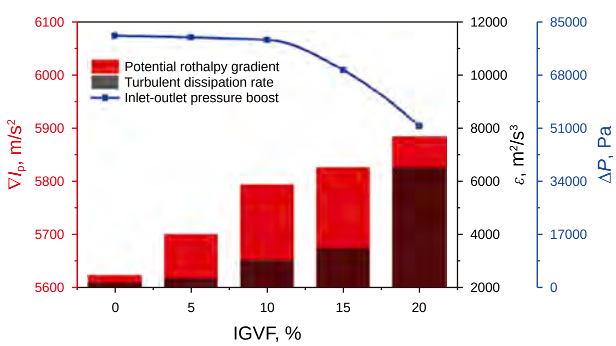

Fig. 21. Distributions of potential rothalpy gradient, turbulent dissipation rate, and pressure boost at pump inlet/outlet.

as secondary flow. Furthermore, as the inlet flow rate increases from 0.6*Q* to 1.0*Q*, the SI value at the impeller outlet gradually decreases to 0.59. At 1.2*Q*, the SI value at the impeller outlet increases to 0.68, while the SI value at the guide vane outlet decreases to 0.52. When the flow rate increases to 1.4*Q*, the SI value at the impeller outlet rises to 0.77, and the SI value at the guide vane outlet increases to 0.6.

It can be seen that the inlet flow rate significantly affects the flow characteristics in the vane-type multiphase pump, and adjusting the flow rate can effectively control the internal flow of hydraulic machinery. In practical operation, the secondary flow diagnostic theory can effectively identify the flow stability state of the vane-type multiphase pump under different operating conditions. It is found that under gas-liquid two-phase conditions, the outflow condition at the design flow rate is relatively the most stable, and the total energy loss at the outlet of the pressure-boosting unit is the lowest. This also provides a more accurate theoretical basis for the optimized operation of the vane-type multiphase pump.

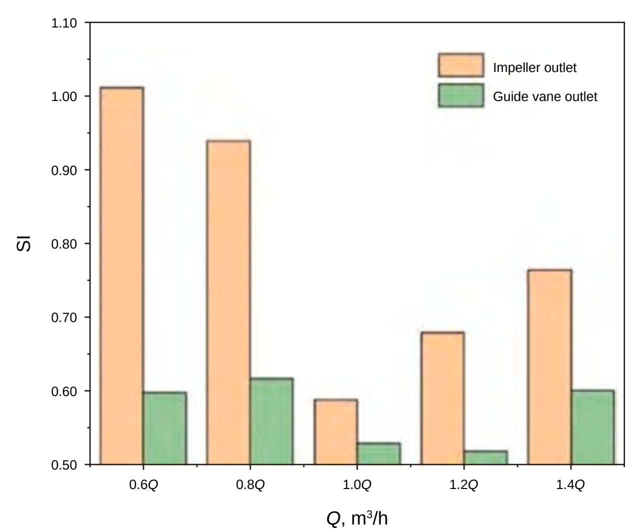

Fig. 22. SI value distribution at impeller/guide vane outlets under different flow rates.

5.4. Vortex decomposition and energy loss in the vane-type multiphase pump

Fig. 23 shows the distribution of axial vortices, circumferential vortices, radial vortices, and tip clearance streamlines under pure water conditions. From Fig. 23, it can be observed that the tip clearance streamlines flow out from the leading edge of the tip clearance and move circumferentially along the passage to the outlet position, forming a long strip of TLV. Among the components of the TLV, the circumferential vortex accounts for the largest proportion compared to the axial and radial vortices, making it the main component of the TLV. At the same time, in the front TLV region, the vortex components are mainly circumferential vortices, while axial vortices begin to appear in the middle breakage region of the leakage vortex, where the kink degree of the jet streamlines is relatively low. In addition, near the shear band of the leakage vortex, the jet from the adjacent passage flows in through the clearance and intertwines with the main flow, forming the middle part of the leakage vortex. Axial vortices are mainly concentrated near the leading edge of the blade pressure side and the tail region of the leakage vortex. Circumferential vortices account for the largest proportion of the leakage vortex and are therefore the main component, while radial vortices account for the smallest proportion and are mainly distributed in local regions near the leading and trailing edges of the blade. Furthermore, when the fluid passes through the narrowest part of the passage, the axial vortices in the passage are relatively severe. At the same time, when the tail of the leakage vortex experiences flow separation and dissipation, the proportion of the axial component of the vortex is also large, which fully indicates that the axial component plays a certain driving role in the generation and collapse of the vortex.

Fig. 24 shows the distribution of axial vortices, circumferential vortices, radial vortices, and tip clearance streamlines at an inlet gas volume fraction of 10%. From Fig. 24, it can be seen that under gas-liquid two-phase conditions, the leakage jet streamlines are more densely distributed in the passage, and there are relatively fewer jets in the shear band. Near the clearance in the shear band region, obvious gas accumulation occurs, and in most regions near the trailing edge clearance of the blade, the gas volume fraction is very high. It can also be seen from Fig. 24 that compared to the pure water condition, the distribution of axial vortices at the tail of the leakage vortex gradually increases under gas-liquid two-phase conditions, meaning that the axial component gradually increases when the vortex sheds and dissipates. In the front and rear sections of the leakage vortex, the vortex scale of the circumferential vortex is significantly larger, but the vortex intensity of the circumferential vortex begins to decrease in local regions in the middle of the leakage vortex. This is caused by local gas blockage in the clearance, which reduces the velocity of the clearance jet at this position and prevents it from forming strong convection with the main flow on the pressure side, thereby affecting the diffusion of the circumferential vortex to some extent. It can be concluded that axial and circumferential vortices are the main components of the vortex, and the presence of gas significantly increases the distribution of axial and circumferential vortices throughout the impeller region.

The preceding analysis has identified the core positions of tip leakage vortices in the vane-type multiphase pump. The following section will conduct an in-depth analysis of the correlation between energy loss and vortex intensity at the vortex core, with quantitative analysis revealing their relationship patterns.

Fig. 25 shows the distribution of circumferential vortices, axial vortices, and energy loss along the vortex core under 10% gas volume fraction. From Fig. 25, it can be observed that along the vortex axis of the TLV, the variation patterns of rigid vorticity for both circumferential and axial vortices at different spatial positions correspond with energy loss distribution.

In the P_1–P_4 interval, the rigid vorticity of both circumferential and axial vortices gradually decreases from 7844 s^{-1} and 666 s^{-1} to 1187 s^{-1} and 491 s^{-1} respectively, while the entropy production rate at the vortex core correspondingly drops from 13,783 to 4665 W/(m^3·K). During the P_4–P_6 interval, both axial and circumferential vortices at the vortex core begin to increase, with axial vortices showing the most rapid growth. Concurrently, the entropy production rate rises to 18,711 W/(m^3·K), indicating that the axial vortex growth at P_6 contributes significantly to energy loss. Point P_6 is located at the leading edge of the blade suction side, where both axial and circumferential vortices are most densely distributed—the primary reason for its maximum energy loss. In the P_6–P_9 interval, the rigid vorticity of both axial and circumferential vortices gradually decreases, accompanied by a substantial reduction in energy loss. However, from P_9 to P_{10}, as the leakage vortex enters the rear leakage vortex stage, large-scale vortex shedding occurs in the flow passage, leading to significant energy loss and consequent increase in entropy production rate.

5.5. Transient characteristics of TLV and gas phase in vane-type multiphase pump

Fig. 26 shows the distribution of circumferential vortices, axial vortices, and gas phase in the impeller passage under different flow rates at an inlet gas volume fraction of 10%. From Fig. 26, it can be observed that at 0.8*Q* flow rate, the leading edge of the blade suction side fails to form a stable structure, and the pressure side is dominated by circumferential vortices. The inlet circumferential velocity is relatively low, but vortex and gas phase concentrations increase

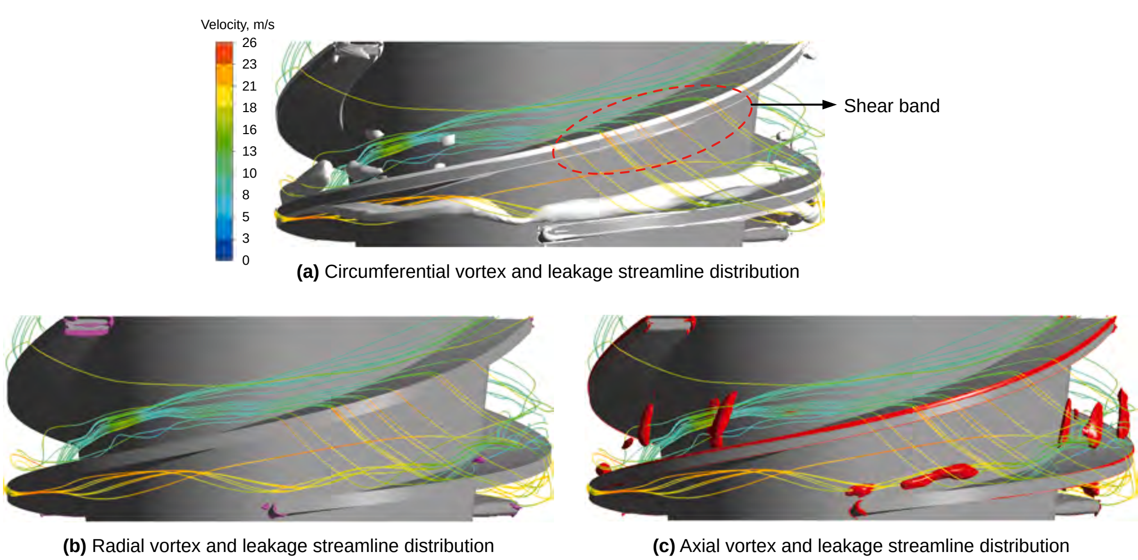

Fig. 23. Axial, circumferential, and radial vortices with tip clearance streamlines (IGVF = 0%).

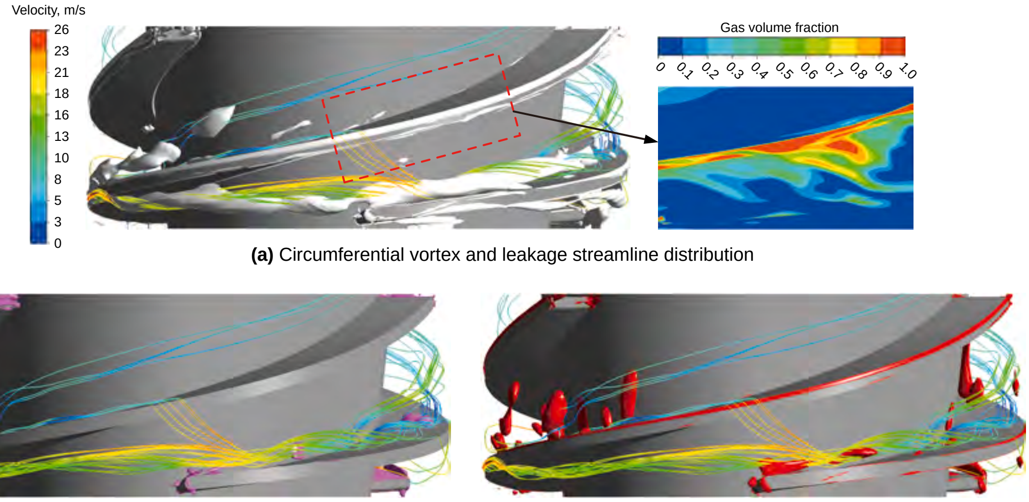

(a) Circumferential vortex and leakage streamline distribution

(b) Radial vortex and leakage streamline distribution

(c) Axial vortex and leakage streamline distribution

Fig. 24. Spatial distribution of axial/circumferential/radial vortices and tip clearance streamlines (IGVF = 10%).

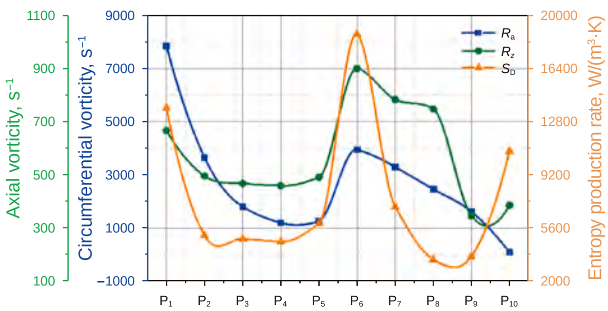

Fig. 25. Circumferential/axial vortices and energy loss along vortex cores.

near the passage outlet. When the flow rate increases to 1.0Q, the leakage vortex at the suction side leading edge gradually forms, but breakage occurs near the pressure side leading edge. At this stage, axial vortices become more prominent at the pressure side leading edge and mid-region, while both circumferential and axial velocities increase. Notably, at the passage inlet, the circumferential velocity decreases toward the tip region across all cross-sections. This velocity gradient-induced shear effect significantly enlarges the scale of circumferential vortices. Under 1.2Q flow rate, axial vortices in the passage gradually diminish, and the distribution of circumferential vortices shifts toward the suction side. Concurrently, the leakage vortex no longer exhibits significant breakage, and the circumferential vortices near the pressure side leading edge closely approach the suction side of adjacent blades.

The above analysis reveals that at low flow rates, circumferential and axial vortices are constrained by the shear effects of circumferential and axial velocities, resulting in smaller vortex scales of the leakage vortex, with distribution limited to the vicinity of the blade pressure side leading edge. At the design flow rate, the distribution of axial vortices gradually increases in the tail region of the leakage vortex, while circumferential vortices become significantly more concentrated near the suction side leading edge. However, distinct breakage and instability zones emerge under these conditions. At high flow rates, the inlet velocity increases, but the circumferential velocity variation near the suction side leading edge remains minimal. The initiation position of the leakage vortex shifts downward, with circumferential vortices predominantly distributed along the suction side, effectively preventing breakage in the mid-region of the leakage vortex.

These findings demonstrate that flow rate significantly influences vortex distribution and gas-liquid separation characteristics. At low flow rates, the TLV remains relatively small, whereas at design and high flow rates, the TLV becomes more pronounced. Furthermore, the degree of gas phase accumulation in the flow passage is strongly affected by vortex behavior. Therefore, this section focuses on analyzing the transient evolution of the TLV and gas phase at design and high flow rates.

Fig. 27 illustrates the three-dimensional spatiotemporal evolution of vortices and the gas phase at a flow rate of 1.0Q. From Fig. 27, it can be observed that at 1.0Q, the distribution of circumferential vortices in the impeller passage aligns with the gas phase at different time instants. At 0.4131 s, circumferential vortices form near the blade suction side, while axial vortices, radial vortices, and gas phase distribution remain minimal. By 0.4164 s, the circumferential vortices gradually shift toward the pressure side, and the vortex regions of the front and middle leakage vortices begin compressing toward the mid-region, forming a breakage zone. The vortex axis in the circumferential direction moves in opposite directions, ultimately leading to breakage at 0.42 s.

During the period T = [0.4131 s, 0.42 s], axial vortices diffuse from the leading edge toward the outlet. As the breakage zone develops, both circumferential and axial vortices progressively increase in the flow passage, accompanied by a growing concentration of gas phase within the vortices. This indicates that vortex diffusion and growth intensify gas phase accumulation in the passage.

Fig. 28 shows the three-dimensional spatiotemporal evolution of vortices and gas phase at a flow rate of 1.2Q. From Fig. 28, it can be observed that compared to the 1.0Q flow rate, the variation of vortices in the flow passage over time is smaller at 1.2Q. The initial position of circumferential vortices is relatively delayed. During the period T = [0.4131 s, 0.4164 s], circumferential vortices gradually diffuse toward the middle of the flow passage, with their scale significantly increasing. Meanwhile, the gas phase exhibits a tubular distribution and is entrained by the vortices toward the outlet. At 0.42 s, the scale of circumferential vortices gradually decreases, and the distribution area of the gas phase also reduces. However, the structure of the TLV remains stable without breakage. Fig. 28 also reveals that at 1.2Q flow rate, axial vortices are less distributed, and

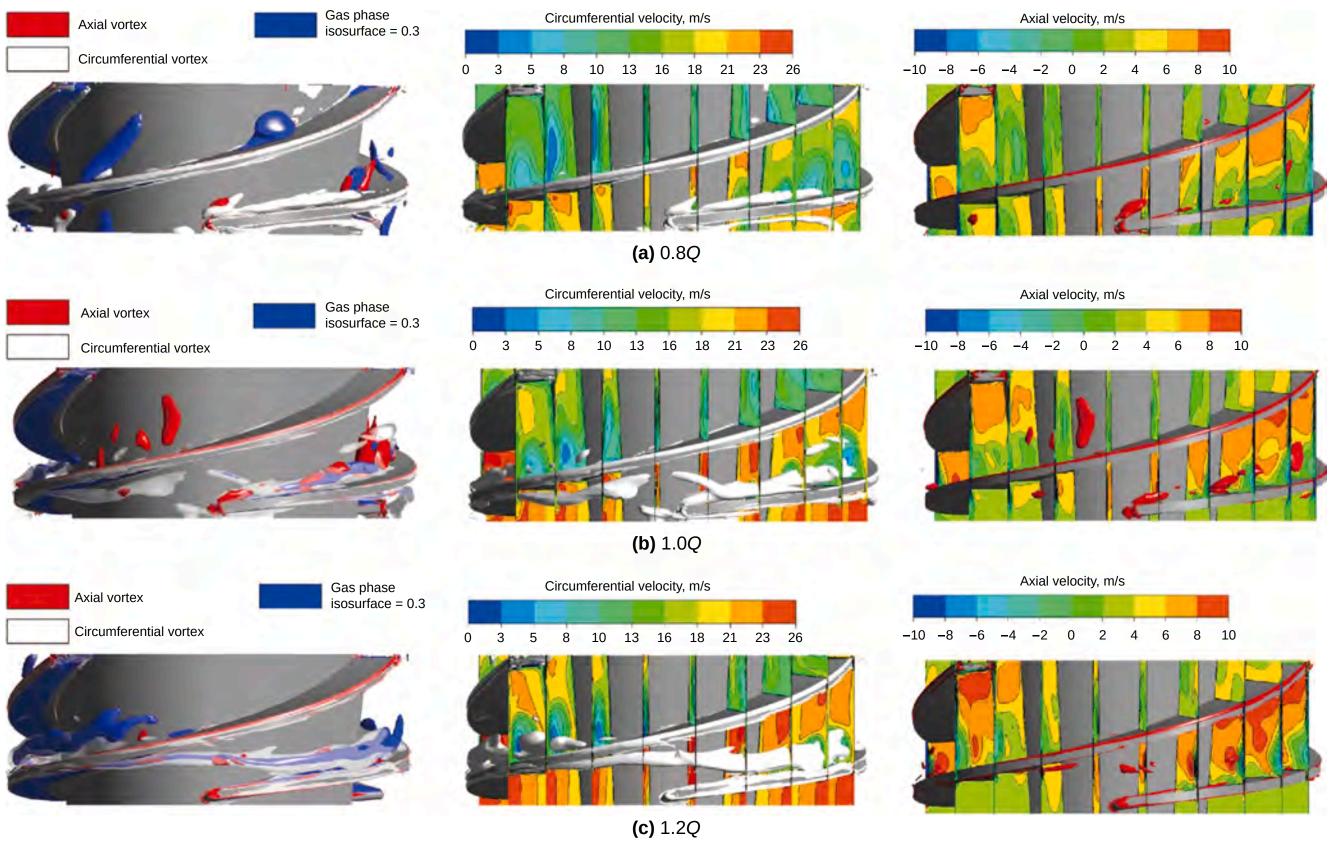

Fig. 26. Distributions of circumferential/axial vortices and gas phase (IGVF = 10%).

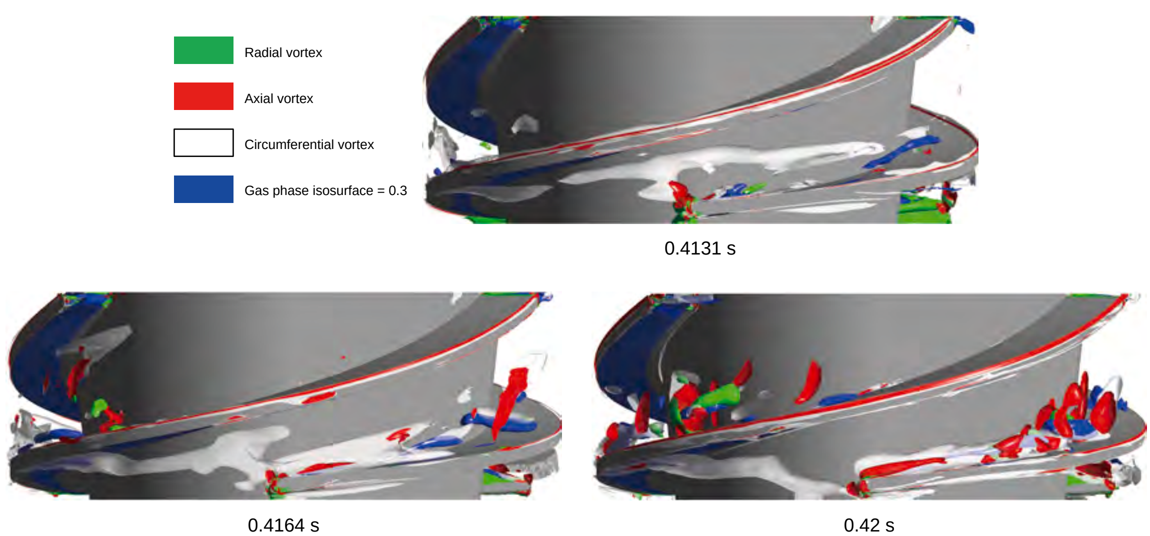

Fig. 27. 3D spatiotemporal evolution of vortices and gas phase at 1.0Q flow rate (IGVF = 10%).

their increase is slow during T = [0.4131 s, 0.42 s]. Circumferential vortices exhibit an elongated distribution, and vortex shedding in the rear leakage vortex region is minimal, which is related to the slower development of axial vortices in the flow passage.

In summary, as the inlet flow rate increases, both the circumferential and axial velocities in the shroud region of the flow passage also increase, thereby influencing the positional changes of the TLV. The continuous dissipation and regeneration of axial and circumferential vortices over time further entrain the gas phase toward the outlet, demonstrating that the spatiotemporal evolution characteristics of vortices significantly affect gas-liquid two-phase transport.

5.6. *Pressure pulsation characteristics in vane-type multiphase pump*

In studies concerning pressure pulsations in vane-type multiphase pumps, Wen et al. (2022) found a strong correlation between

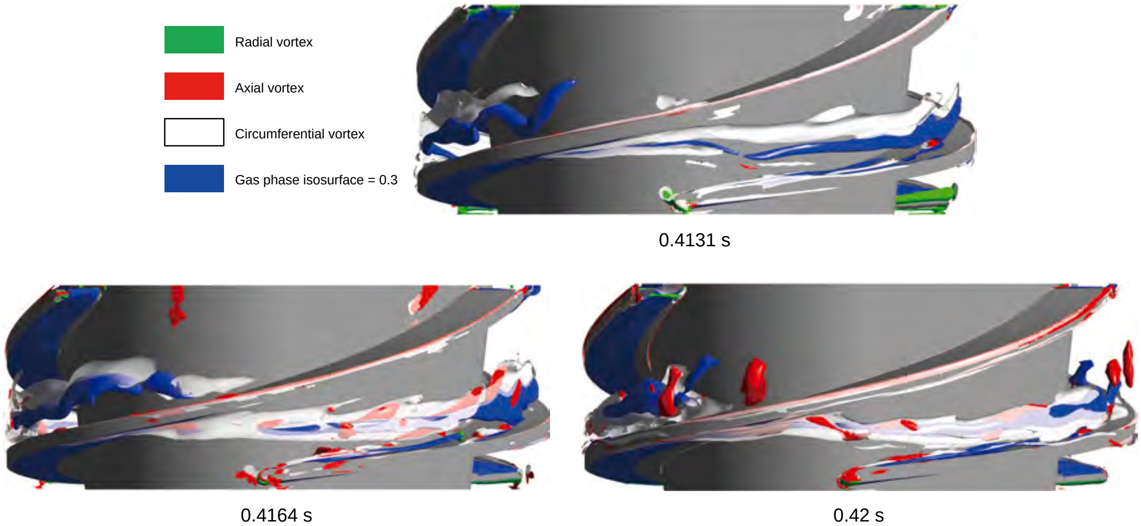

Fig. 28. 3D spatiotemporal evolution of vortices and gas phase at 1.2Q flow rate (IGVF = 10%).

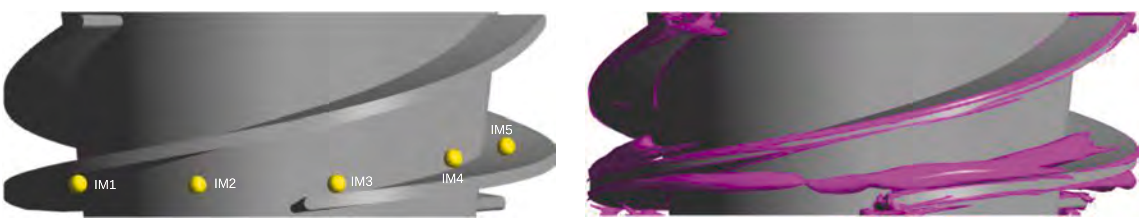

Fig. 29. Monitoring points in impeller flow passage.

tip leakage vortices and pressure pulsations. Therefore, the following analysis takes monitoring points at the core positions of tip leakage vortices at different locations to examine the relationship between pressure pulsations and circumferential/axial vortices.

Fig. 29 shows monitoring points (IM1~IM5) in the core region of the TLV under one operating condition. These points will vary with changes in the vortex core center under different conditions. All five points are located along the vortex axis of the TLV, with IM2 in the front leakage vortex region, IM3-IM4 in the middle leakage vortex region, and IM5 in the rear leakage vortex region. This section conducts an in-depth analysis of pressure pulsations at these five points to reveal patterns in frequency and time domain variations under different operating conditions.

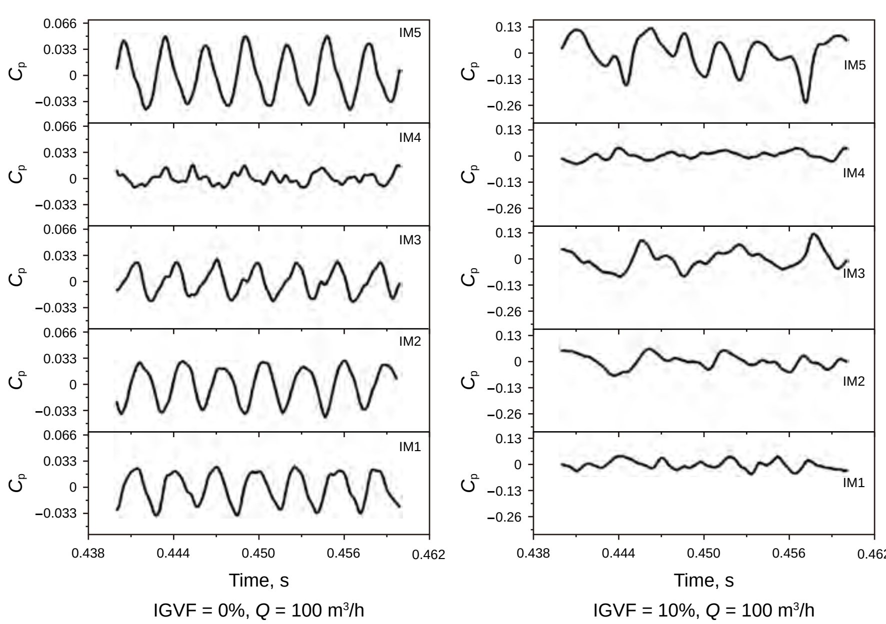

Fig. 30. Time-domain diagrams of monitoring points under pure water and two-phase conditions.

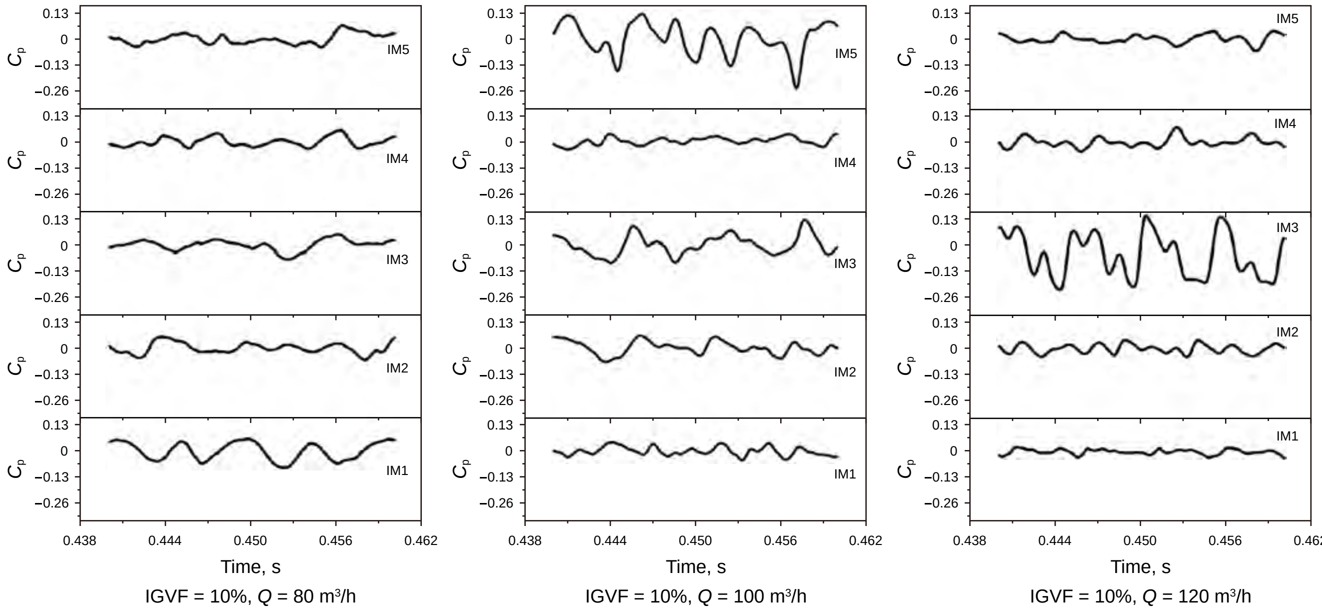

Fig. 31. Time-domain diagrams of monitoring points at different flow rates.

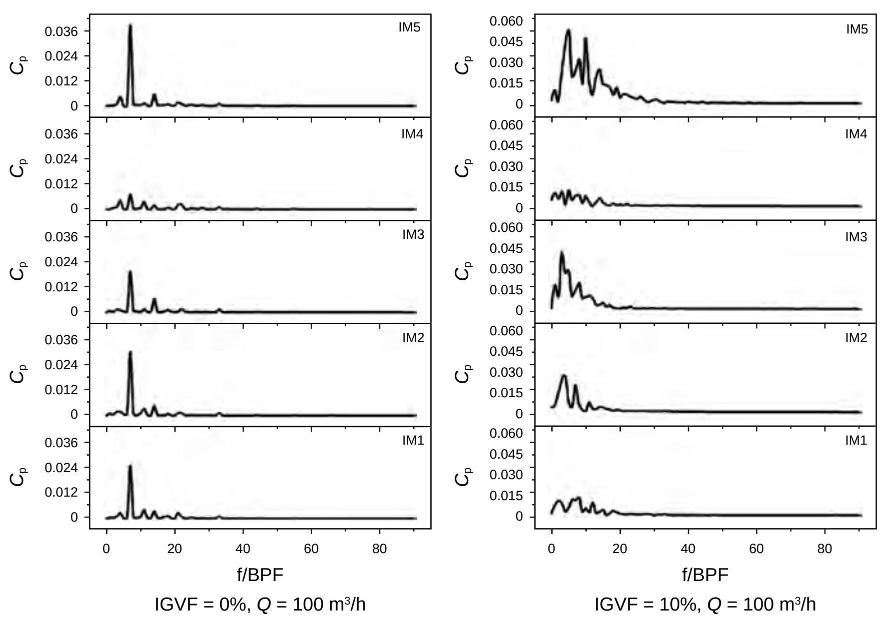

Fig. 32. Frequency-domain diagrams of monitoring points under pure water and two-phase conditions.

Fig. 30 shows the time-domain diagrams of monitoring points in the impeller under pure water and gas-liquid two-phase conditions. From Fig. 30(a), it can be observed that under pure water conditions, the maximum pressure pulsation amplitudes at IM1~IM5 are 0.0264, 0.03093, 0.02723, 0.01666, and 0.0489, respectively. IM1 and IM2 represent two positions in the front leakage vortex, with IM2 located in the vortex diffusion region, exhibiting relatively higher pressure pulsation amplitudes. IM3 is near the pressure side leading edge of the blade, where both axial and circumferential vortices are densely distributed, resulting in higher pressure pulsation amplitudes. IM5 is situated in the region where large-scale shedding of the TLV occurs, corresponding to the highest pressure pulsation amplitude.

From Fig. 30(b), under gas-liquid two-phase conditions, the maximum pressure pulsation amplitudes at IM1~IM5 are 0.04521, 0.06642, 0.125, 0.041, and 0.124, respectively. The presence of the gas phase significantly increases the pressure pulsation amplitudes at the same vortex core positions, particularly at IM3 and IM5, which are located near the suction side leading edge and mid-region.

Fig. 31 shows the time-domain diagrams of monitoring points in the impeller under different flow rates. From Fig. 31(a), it can be observed that compared to the design flow rate, the pressure pulsation amplitudes at monitoring points IM2~IM5 are lower at 0.8Q flow rate, which is attributed to the relatively fewer vortices in these four regions. However, the maximum pressure pulsation amplitude at IM1 is higher, resulting from the elevated SI value at the impeller inlet under low flow rate conditions.

From Fig. 31(c), at high flow rates, the maximum pressure pulsation amplitudes at IM1~IM5 are 0.02357, 0.04352, 0.22902, 0.07462 and 0.03918, respectively. The pressure pulsation amplitudes at IM3 and IM4 are notably higher, with IM3 exhibiting the highest amplitude, as it is located in a vortex-concentrated region. IM3 is situated near the pressure side leading edge of the blade, where both axial and circumferential vortices are densely distributed, leading to higher pressure pulsation amplitudes. In contrast, IM1, IM2 and IM5 are positioned in regions dominated by circumferential vortices with fewer axial vortices, resulting in relatively lower pressure pulsation amplitudes. Additionally, under high flow rate conditions, the variation of vortices in the impeller passage over one cycle is minimal, and the overall fluctuation in pressure pulsation amplitudes is smaller.

Fig. 32 presents the frequency-domain analysis of monitoring points under design flow rate conditions for both pure water and 10% inlet gas volume fraction. From Fig. 32, it can be observed that under pure water conditions, the pressure pulsation amplitudes at monitoring points IM1~IM6 are concentrated at 6 times the rotational frequency, with IM4 and IM5 exhibiting the minimum and maximum pressure pulsation amplitudes, respectively. The secondary high-amplitude pressure pulsation frequencies at IM1~IM5 are rare, indicating that high-amplitude pressure pulsations under pure water conditions have short durations.

Under gas-liquid two-phase conditions, the dominant frequency at IM1 occurs at 7 times the rotational frequency, while IM2 and IM3 show dominant frequencies at 3 times, and IM4 and IM5 at 5 times the rotational frequency. This demonstrates that pressure pulsations under gas-liquid conditions are concentrated in low-frequency ranges, meaning the gas phase intensifies low-frequency disturbances in the impeller region.

Fig. 33 shows the frequency-domain analysis of monitoring points under different flow rates at 10% inlet gas volume fraction. From Fig. 33, it can be seen that at 0.8Q flow rate, the dominant frequencies at IM1, IM2, and IM3 are 4, 5, and 3 times the rotational frequency, respectively, while IM4 and IM5 are concentrated at 5 and 2 times the rotational frequency. Compared to the design flow rate, the dominant frequencies at IM1 and IM5 are lower at 0.8Q. When the flow rate increases to 1.2Q, the dominant frequencies at IM1, IM2, and IM3 all occur at 4 times the rotational frequency, while IM4 and IM5 are concentrated at 8 and 7 times, respectively. The pressure pulsation amplitude at IM3 increases, whereas the amplitudes at other points decrease significantly.

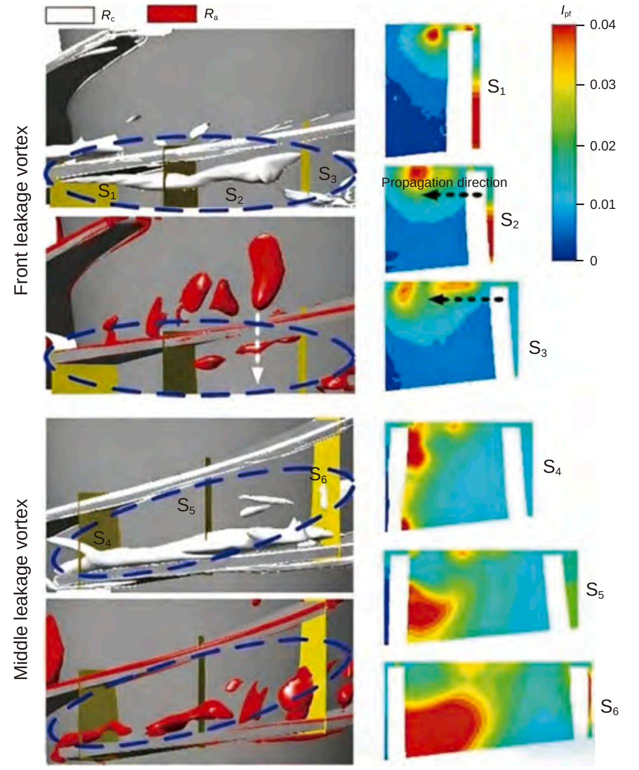

Fig. 34. Correlation between TLV and pressure pulsation intensity under two-phase conditions.

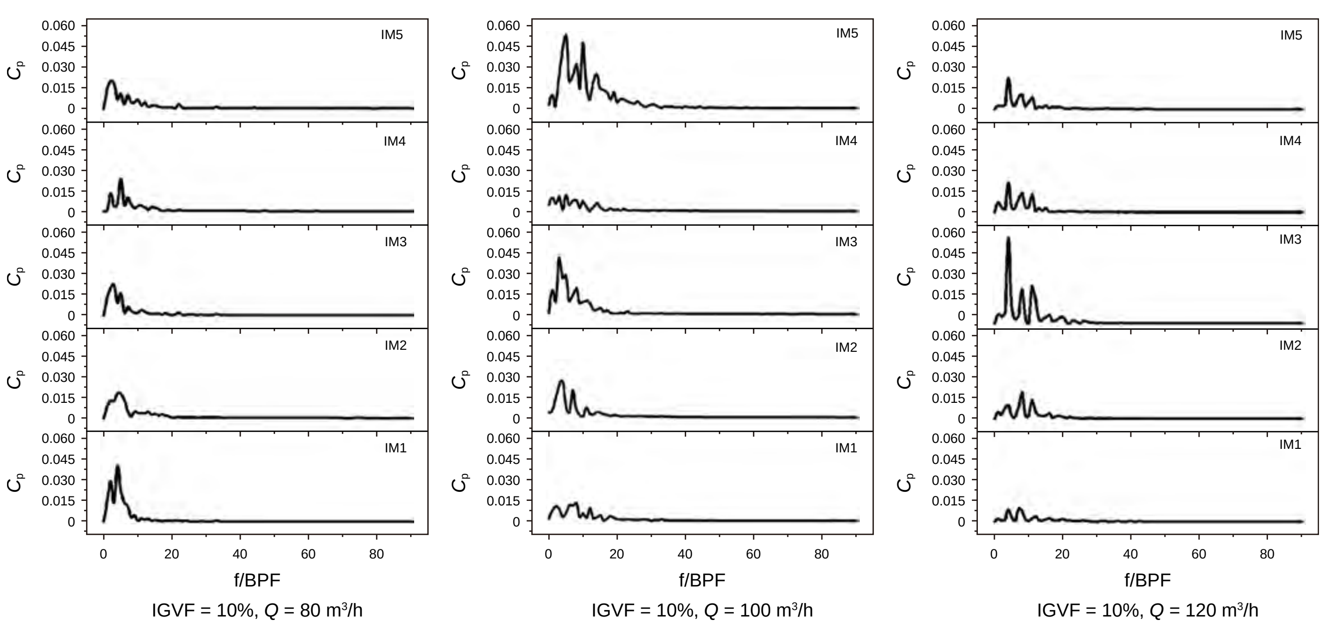

Fig. 33. Frequency-domain diagrams of monitoring points at different flow rates.

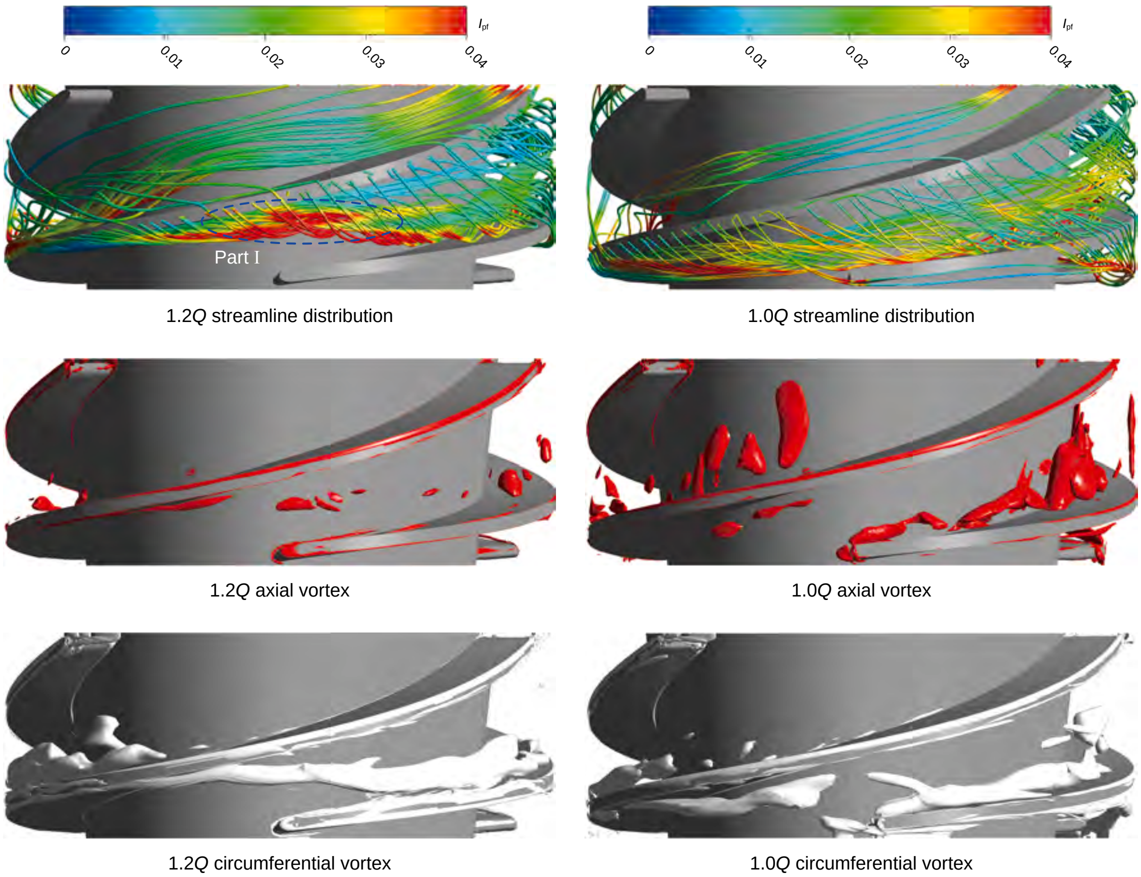

Fig. 35. Vortex/streamline/pressure pulsation intensity distributions at different flow rates.

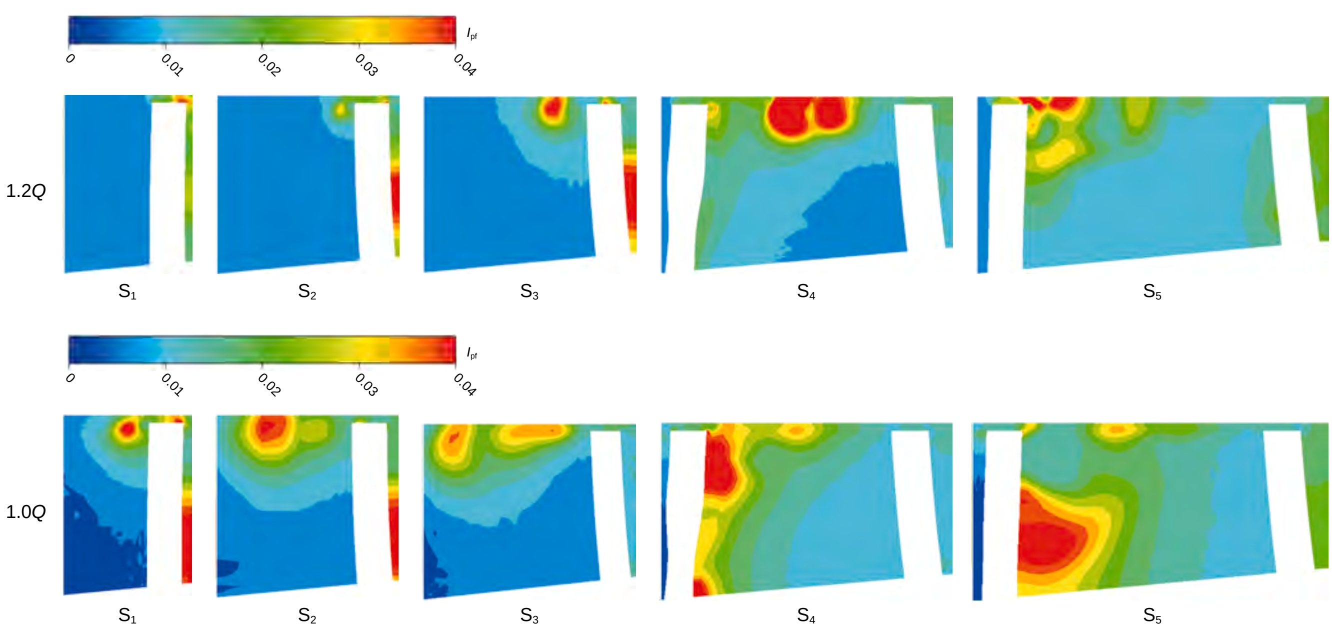

Fig. 36. Pressure pulsation intensity distributions at cross-sections under different flow rates (IGVF = 10%).

This indicates that at low flow rates, the dominant and secondary frequencies at all five monitoring points are below 19 times the rotational frequency, and their amplitudes are notably lower than those under the other two flow conditions except for IM1, which is closely related to the distribution of leakage vortices in the impeller passage. Under low flow conditions, the pressure amplitudes near the suction side inlet of the impeller are higher and concentrated in low frequencies, which can cause significant damage to the vane-type multiphase pump. As the inlet flow rate increases, the pressure pulsation amplitudes at the suction side inlet gradually decrease.

Fig. 33 also reveals that at 0.8*Q*, the pressure pulsation amplitudes at the dominant frequencies of the other four points (excluding IM1) are generally low, which is associated with the reduced presence of tip leakage vortices in the flow passage. In contrast, at 1.0*Q* and 1.2*Q*, the pressure pulsation amplitudes are higher and concentrated in regions with dense leakage vortex distributions, demonstrating an inseparable link between vortex distribution and pressure pulsations. Adjusting the flow rate to control tip leakage vortices, thereby reducing pressure pulsations in the flow passage, provides valuable guidance for improving the performance of multiphase pumps.

In summary, under off-design operating conditions, pressure pulsations at the core of the TLV are mostly concentrated in low frequencies with smaller amplitudes at low flow rates, whereas at high flow rates, local regions exhibit larger low-frequency pressure pulsation amplitudes. This phenomenon is strongly correlated with the evolution and distribution of leakage vortices.

5.7. Correlation between TLV and pressure pulsation intensity

Fig. 34 shows the distribution of tip leakage vortices and pressure pulsation intensity under gas-liquid two-phase conditions. From Fig. 34, it can be observed that during the front leakage vortex stage, the distribution of pressure pulsation intensity aligns with that of circumferential vortices. At the impeller inlet, the TLV primarily consists of circumferential vortices, which exhibit an elongated distribution, while axial vortices appear as fragmented strips. From cross-section S_2 to S_3, as axial vortices emerge, the pressure pulsation intensity eventually forms two concentrated regions at cross-section S_3. The high-pressure pulsation region gradually expands along the flow direction, primarily due to the increasing scale of circumferential vortices. This expansion is closely linked to the growth of vortex structures and their interaction with the surrounding flow field. The results highlight the significant influence of circumferential vortices on pressure pulsation characteristics in multiphase pumping systems.

Fig. 34 further reveals that during the middle leakage vortex stage, both circumferential and axial vortices coexist. Here, circumferential vortices concentrate near the shroud, entraining the medium toward the outlet. At cross-section S_5, the scale of axial vortices begins to increase, accompanied by an expansion of high-pressure pulsation intensity regions, which are distributed closer to the hub.

At cross-section S_6, the TLV appears in a shedding form. In this region, circumferential vortices gradually decrease while axial vortices increase in both distribution and volume. Concurrently, pressure pulsations intensify in the terminal region of the middle leakage vortex, exhibiting a diffusion trend consistent with axial vortices. Under conditions of 1.0*Q* flow rate and 10% inlet gas volume fraction, the growth of axial vortices indicates vortex shedding in this area. Such shedding exacerbates secondary flow disturbances and further influences pressure pulsation variations.

The analysis demonstrates that different vortex types dominate pressure pulsation intensity at various locations in the vane-type multiphase pump impeller. The front leakage vortex region is primarily influenced by circumferential vortices driving pressure pulsation changes, while the middle leakage vortex region is mainly affected by axial vortices causing pressure pulsation variations.

Fig. 35 displays the distribution of vortices, streamlines, and pressure pulsation intensity under different flow rates at 10% gas volume fraction. At 1.2*Q* flow rate, the tip leakage streamlines concentrate along the mid-section of the blade suction side. Compared to the design flow rate, pressure pulsation intensity is notably lower during the front leakage vortex stage. In the middle leakage vortex section, however, the pressure intensity of clearance streamlines remains significantly high. Axial and circumferential vortices in Part I show distinct behavior: axial vortices reduce substantially at high flow rates, while circumferential vortices maintain structural integrity without breakage—key factors underlying the region's pronounced pressure pulsation intensity. Conversely, at the design flow rate, pressure pulsation intensity peaks at both the front and rear sections of the leakage vortex. The front section shows dominance of circumferential vortex components, while the rear section experiences large-scale vortex shedding with dramatically multiplied axial vortices. These findings underscore how flow rate modulates vortex morphology and its cascading effects on pressure pulsation characteristics, providing critical insights for operational optimization of multiphase pumps.

Fig. 36 shows the distribution of pressure pulsation intensity at various cross-sections within the impeller passage under different flow rates. From Fig. 36, it can be observed that at high flow rates, the pressure pulsation intensity from cross-section S_1 to S_3 is lower than that at the design flow rate. At cross-section S_4, the pressure pulsation intensity concentrates near the shroud in the middle of the flow passage, where it increases due to vortex influence. At cross-section S_5 under high flow conditions, the concentrated region of pressure pulsation intensity shrinks from circular to small patches and distributes near the blade tip. Combined with Fig. 35, it is evident that this region has fewer axial vortices and less vortex shedding.

In summary, when both axial and circumferential vortices increase simultaneously, the pressure pulsation intensity rises. Adjusting the flow rate can effectively control vortex intensity, thereby reducing pressure pulsation intensity in localized regions.

6. Conclusions

(1) In vane-type multiphase pumps, the TLV breaks into segments at design flow rates, forming front, middle, and rear leakage vortices. Vortex strength weakens along the core path and dissipates through shedding. Circumferential velocity governs both vortex instability and strong-weak transition during development.

(2) At 10% gas content, mutual compression between strong vortices causes leakage vortex breakage. The blade pressure side shows higher potential rothalpy gradients, triggering limited secondary flows. Increasing gas content (0–20%) raises turbulent dissipation but reduces pressure boost. Flow rate changes (0.6*Q*–1.4*Q*) cause SI values at outlets to first drop then rise, with poor flow uniformity under off-design conditions.

(3) Under pure water, axial and circumferential vortices dominate, with circumferential vortices being primary in leakage structures. Both correlate with energy loss. Gas presence intensifies both vortex types, especially axial vortices near the pressure side leading edge, causing significant energy loss. Higher flow rates amplify velocity gradients, altering vortex evolution. Circumferential vortex strength increases with gas accumulation, while axial vortex development affects gas distribution.

(4) Gas-liquid operation generates stronger low-frequency pressure pulsation at vortex cores than pure water. Pulsation patterns vary with flow rates: low rates yield smaller amplitudes, while high rates enhance pulsation in middle leakage regions. Circumferential vortices dominate front leakage pulsation, while axial vortices control middle

leakage pulsation. High flow rates reduce pulsation in front/rear regions due to fewer vortices and suppressed shedding, except where unbroken vortices persist.

CRediT authorship contribution statement

Hai-Gang Wen: Writing – review & editing, Writing – original draft, Validation, Supervision. **Guang-Tai Shi:** Project administration, Funding acquisition. **Wen-Juan Lv:** Writing – original draft, Supervision, Formal analysis, Conceptualization. **Hao Qin:** Investigation, Data curation.

Declaration of competing interest

The authors declare that they have no known competing financial interests or personal relationships that could have appeared to influence the work reported in this paper.

Acknowledgments

The authors acknowledge financial support from the Sichuan Natural Science Foundation Outstanding Youth Science Foundation (2024NSFJQ0012), Key project of Regional Innovation and Development Joint Fund of National Natural Science Foundation of China (U23A20669), Sichuan Science and Technology Program (2022ZDZX0041).

Nomenclature

ρ	Density of the medium, kg/m^3
p	Pressure, Pa
t	Time, s
V	Velocity vector, m/s
u_i	Velocity components in the x, y, and z directions, m/s
u_j	Velocity components in the x, y, and z directions, m/s
f_i	Body force term
μ	Dynamic viscosity, Pa·s
I	Total rothalpy, m^2/s^2
I_p	Potential rothalpy, m^2/s^2
I_k	Kinetic rothalpy, m^2/s^2
ω_i	Impeller angular velocity, rad/s
Q_r	Second invariant of the velocity gradient tensor, s^{-2}
ω_R	Rigid vorticity, s^{-1}
Ω_R	relative vortex intensity, s^{-1}
λ_ci	Imaginary part of the complex conjugate eigenvalues of the velocity gradient tensor, s^{-1}
ω	Vorticity vector, s^{-1}
r	Vortex axis direction
C_p	Pressure coefficient
P_i	Instantaneous pressure, Pa
$\overline{P}$	Time-averaged pressure, Pa
U_tip	Impeller inlet velocity, m/s
I_pf	Pressure pulsation intensity

Subscript

TLV	Tip leakage vortex
PRG	Potential rothalpy gradient
DNS	Direct numerical simulation
RANS	Reynolds-averaged Navier-Stokes

References

Cao, F., Shu, P.C., Xing, Z.W., 1999. Advance in study of twin-screw type multiphase pump. China Petrol. Machin. 27 (3), 49–52. https://doi.org/10.3969/j.issn.1001-4578.1999.03.017 (in Chinese).

Cheng, L.X., Chen, T.K., 1999. Performance and research status of multiphase flow mixed-transport pumps. Oil Field Equip. 28 (5), 22–25. https://doi.org/10.3969/j.issn.1001-3482.1999.05.006 (in Chinese).

Cui, B.L., Zhang, C.L., Zhang, Y.L., et al., 2020. Influence of cutting angle of blade trailing edge on unsteady flow in a centrifugal pump under off-design conditions. Appl. Sci. 10 (2), 580. https://doi.org/10.3390/app10020580.

Dong, X.R., Gao, Y.S., Liu, C.Q., 2019. New normalized rortex/vortex identification method. Phys. Fluids 31 (1), 11701. https://doi.org/10.1063/1.5066016.

Feng, J.J., Luo, X.Q., Guo, P.C., et al., 2016. Influence of tip clearance on pressure fluctuations in an axial flow pump. J. Mech. Sci. Technol. 30 (4), 1603–1610. https://doi.org/10.1007/s12206-016-0315-2.

Furukawa, M., Inoue, M., Saiki, K., et al., 1999. The role of tip leakage vortex breakdown in compressor rotor aerodynamics. J. Turbomach. 121 (3), 469–480. https://doi.org/10.1115/1.2841339.

Gao, Y.S., Liu, J.M., Yu, Y.F., et al., 2019. A Liutex based definition and identification of vortex core center lines. J. Hydrodyn. 31 (3), 445–454. https://doi.org/10.1007/s42241-019-0048-7.

Ji, L.L., Li, W., Shi, W.D., et al., 2020. Energy characteristics of mixed-flow pump under different tip clearances based on entropy production analysis. Energy 199, 117447. https://doi.org/10.1016/j.energy.2020.117447.

Ji, L.L., Li, W., Shi, W.D., et al., 2021. Effect of blade thickness on rotating stall of mixed-flow pump using entropy generation analysis. Energy 236, 121381. https://doi.org/10.1016/J.ENERGY.2021.121381.

Lee, J., Kim, Y., Khosronejad, A., et al., 2020. Experimental study of the wake characteristics of an axial flow hydrokinetic turbine at different tip speed ratios. Ocean Eng. 196, 106777. https://doi.org/10.1016/j.oceaneng.2019.106777.

Li, Y.J., Shen, J.F., Liu, Z.Q., et al., 2013. Large eddy simulation of unsteady flow in tip clearance of axial-flow pumps. Trans. Chin. Soc. Agric. Mach. 44 (S1), 113–118. https://doi.org/10.6041/j.issn.1000-1298.2013.S1.021 (in Chinese).

Li, B.W., Li, X.J., Jia, X.Q., et al., 2019. The role of blade sinusoidal tubercle trailing edge in a centrifugal pump with low specific speed. Processes 7 (9), 625. https://doi.org/10.3390/pr7090625.

Li, B., Lu, Q., Jiang, B.Y., et al., 2022. Effects of outer edge bending on the aerodynamic and noise characters of axial fan for air conditioners. Processes 10 (4), 686. https://doi.org/10.3390/PR10040686.

Li, W., Liu, M.J., Ji, L.L., et al., 2023. Study on the trajectory of tip leakage vortex and energy characteristics of mixed-flow pump under cavitation conditions. Ocean Eng. 267, 113225. https://doi.org/10.1016/j.oceaneng.2022.113225.

Ling, G.P., 2000. Research and development of oil-gas multiphase pump technology in China and abroad. J. East China Shipbuild. Inst. 14 (5), 83–87. https://doi.org/10.3969/j.issn.1673-4807.2000.05.019 (in Chinese).

Liu, C.Q., Gao, Y.S., Tian, S.L., et al., 2018. Rortex-A new vortex vector definition and vorticity tensor and vector decompositions. Phys. Fluids 30 (3), 35103. https://doi.org/10.1063/1.5023001.

Liu, M., Tan, L., Cao, S.L., 2019. Dynamic mode decomposition of gas-liquid flow in a rotodynamic multiphase pump. Renew. Energy 139, 1159–1175. https://doi.org/10.1016/j.renene.2019.03.015.

Long, Y., Zhou, Z., Li, N., et al., 2024. Experimental and numerical investigation of tip leakage vortex cavitation in water-jet pump. J. Appl. Fluid Mech. 17 (6), 1191–1203. https://doi.org/10.47176/jafm.17.6.2369.

Lu, H.J., Gao, S.T., 2003. On the helicity and helicity equations. Acta Meteorol. Sin. 61 (6), 684–691. https://doi.org/10.3321/j.issn:0577-6619.2003.06.005 (in Chinese).

Ma, R., Devenport, W.J., 2006. Unsteady periodic behavior of a disturbed tip-leakage flow. AIAA J. 44 (5), 1073–1086. https://doi.org/10.2514/1.12082.

Ma, R., Devenport, W.J., 2007. Tip gap effects on the unsteady behavior of a tip leakage vortex. AIAA J. 45 (7), 1713–1724. https://doi.org/10.2514/1.13536.

Muthanna, C., Devenport, J.W., 2004. Wake of a compressor cascade with tip gap, part 1: Mean flow and turbulence structure. AIAA J. 42 (11), 2320–2331. https://doi.org/10.47176/jafm.17.6.2369.

Nayak, A., Das, D., 2021. Experimental and numerical investigation of flow instability in a transient pipe flow. J. Fluid Mech. 920 (439), A39. https://doi.org/10.1017/JFM.2021.460.

Peng, D., Gregory, J.W., 2015. Vortex dynamics during blade-vortex interactions. Phys. Fluids 27 (5), 53104. https://doi.org/10.1063/1.4921449.

Rashidi, S., Hayatdavoodi, M., Esfahani, J.A., 2016. Vortex shedding suppression and wake control:a review. Ocean Eng. 126, 57–80. https://doi.org/10.1016/j.oceaneng.2016.08.031.

Scheeler, M.W., Reesm, V.W.M., Kedia, H., et al., 2017. Complete measurement of helicity and its dynamics in vortex tubes. Science 357 (6350), 487–491. https://doi.org/10.1126/science.aam6897.

Shen, X., Zhang, D.S., Xu, B., et al., 2021. Experimental and numerical investigation on the effect of tip leakage vortex induced cavitating flow on pressure fluctuation in an axial flow pump. Renew. Energy 163, 1195–1209. https://doi.org/10.1016/j.renene.2020.09.004, 2021.

Shi, G.T., Liu, Z.K., Xiao, Y.X., et al., 2020a. Effect of the inlet gas void fraction on the tip leakage vortex in a multiphase pump. Renew. Energy 150, 46–57. https://doi.org/10.1016/j.renene.2019.12.117.

Shi, G.T., Liu, Z.K., Xiao, Y.T., et al., 2020b. Energy conversion characteristics of multiphase pump impeller analyzed based on blade load spectra. Renew. Energy 157, 9–23. https://doi.org/10.1016/j.renene.2020.04.125.

Shi, G.T., Liu, Z.K., Xiao, Y.X., et al., 2020c. Tip leakage vortex trajectory and dynamics in a multiphase pump at off-design condition. Renew. Energy 150, 703–711. https://doi.org/10.1016/j.renene.2020.01.024.

Shi, W.D., Shao, P.P., Zhang, D.S., et al., 2014. Influence of operating conditions and tip clearance on tip leakage vortex trajectory in axial-flow pumps. J. Drain. Irrigat. Machin. Eng. 32 (5), 373–377. https://doi.org/10.3969/j.issn.1674-8530.13.0085 (in Chinese).

Shi, W.D., Shi, Y., Gao, X.F., et al., 2020d. Simulation and experiment on large particle internal flow characteristics in swirl pump based on DEM-CFD. Trans. Chin. Soc. Agric. Mach. 51 (10), 176–185. https://doi.org/10.6041/j.issn.1000-1298.2020.10.020 (in Chinese).

Shi, G.T., Wang, Z.W., 2019. Pressurization performance of different areas within multiphase pump impeller. J. Drain. Irrigat. Machin. Eng. 37 (1), 13–17. https://doi.org/10.3969/j.issn.1674-8530.18.0102 (in Chinese).

Shi, L., Zhang, D., Jin, Y., et al., 2017. A study on tip leakage vortex dynamics and cavitation in axial-flow pump. Fluid Dyn. Res. 49 (3), 35504. https://doi.org/10.1088/1873-7005/aa6637.

Shu, Z.K., Shi, G.T., Tao, S.J., et al., 2021a. Three-dimensional spatial-temporal evolution and dynamics of the tip leakage vortex in an oil–gas multiphase pump. Phys. Fluids 33 (11), 113320. https://doi.org/10.1063/5.0073634.

Shu, Z.K., Shi, G.T., Yao, X., et al., 2021b. Influence factors and prediction model of enstrophy dissipation from the tip leakage vortex in a multiphase pump. Sci. Rep. 12 (1), 16032. https://doi.org/10.1038/S41598-022-20380-8.

Sun, T., Zhang, H.M., Li, L.C., et al., 2020. Scaling design and analysis of centrifugal compressors. Chin. J. Ship Res. 15 (S1), 141–148. https://doi.org/10.19693/j.issn.1673-3185.01683 (in Chinese).

Turgut, S., Daly, J.J., 1987. Effect of ambient turbulence on trailing vortices. J. Aircraft 24 (6), 399–404. https://doi.org/10.2514/3.45459.

Wang, C.Y., Zeng, Y.S., Yao, Z.F., et al., 2021a. Rigid vorticity transport equation and its application to vortical structure evolution analysis in hydro-energy machinery. Eng. Appl. Comput. Fluid Mech. 15 (1), 1016–1033. https://doi.org/10.1080/19942060.2021.1938685.

Wang, C.Y., Wang, F.J., An, D.S., et al., 2021b. A general alternate loading technique and its applications in the inverse designs of centrifugal and mixed-flow pump impellers. Sci. China Technol. Sci. 64 (4), 898–918. https://doi.org/10.1007/s11431-020-1687-4.

Wen, H.G., Lv, W.J., Shi, G.T., et al., 2022. Effect of the tip clearance on tip leakage vortex and pressure fluctuation characteristics in a helico-axial flow multiphase pump. AIP Adv. 12 (8), 085326. https://doi.org/10.1063/5.0096600.

Wu, H.X., Miorini, L.R., Katz, J., 2012. The internal structure of the tip leakage vortex within the rotor of an axial waterjet pump. J. Turbomach. 134 (3), 403–419. https://doi.org/10.1115/1.4003065.

Wu, Y.F., Zhang, W.H., Wang, Y.F., et al., 2020. Energy dissipation analysis based on velocity gradient tensor decomposition. Phys. Fluids 32 (3), 35114. https://doi.org/10.1063/1.5144424, 035114.

Wu, H.X., Miorini, L.R., Katz, J., 2021. Measurements of the tip leakage vortex structures and turbulence in the meridional plane of an axial water-jet pump. Exp. Fluid 50 (4), 989–1003. https://doi.org/10.1007/s00348-010-0975-0.

Yan, S., Sun, S.H., Luo, X.Q., et al., 2020. Numerical investigation on bubble distribution of a multistage centrifugal pump based on a population balance model. Energies 13 (4), 908. https://doi.org/10.3390/en13040908.

Yao, X.T., Shi, G.T., Liu, Z.K., et al., 2020. Effects of gas volume fraction on the stress and strain of the multiphase pump blade. J. Eng. Therm. Energy Power 35 (8), 45–53. https://doi.org/10.16146/j.cnki.rndlgc.2020.08.007 (in Chinese).

Ye, C., Mehedi, M.M., Kan, K., et al., 2024. Investigation on leakage vortex propagation stability in tip clearance of axial liquid hydrogen pumps. Int. J. Hydrogen Energy 89, 1196–1211. https://doi.org/10.1016/j.ijhydene.2024.09.452.

Yu, Y.F., Shrestha, P., Alvarez, O., et al., 2020. Correlation analysis among vorticity Q method and liutex. J. Hydrodyn. 32 (6), 1207–1211. https://doi.org/10.1007/s42241-020-0069-2.

Zhang, D.S., Wang, H.Y., Shi, W.D., et al., 2014. Experimental study on pressure pulsation characteristics of axial-flow pumps under multiple operating conditions. Trans. Chin. Soc. Agric. Mach. 45 (11), 139–145. https://doi.org/10.6041/j.issn.1000-1298.2014.11.022 (in Chinese).

Zhang, D.S., Shi, W.D., Pan, D.Z., et al., 2015a. Numerical and experimental investigation of tip leakage vortex cavitation patterns and mechanisms in an axial flow pump. J. Fluid Eng. 137 (1), 61–71. https://doi.org/10.1115/1.4030914.

Zhang, D.S., Shi, L., Chen, J., et al., 2015b. Transient characteristics analysis of tip leakage vortex in axial-flow pump based on large eddy simulation. Trans. Chin. Soc. Agric. Eng. 31 (11), 74–80. https://doi.org/10.11975/j.issn.1002-6819.2015.11.011 (in Chinese).

Zhang, J.Y., Cai, S.J., Li, Y.J., et al., 2016. Visualization study of gas–liquid two-phase flow patterns inside a three-stage rotodynamic multiphase pump. Exp. Therm. Fluid Sci. 70, 125–138. https://doi.org/10.1016/j.expthermflusci.2015.08.013.

Zhang, D.S., Shen, X., Dong, Y.G., et al., 2020. Numerical simulation of internal flow characteristics in mixed-flow pumps under different tip clearances. J. Drain. Irrigat. Machin. Eng. 38 (8), 757–763. https://doi.org/10.3969/j.issn.1674-8530.18.0015 (in Chinese).

Zhang, H., Zuo, F.Y., Zhang, D.S., et al., 2021. Formation and evolution mechanisms of tip leakage vortex and vortex cavitation in axial-flow pumps. Trans. Chin. Soc. Agric. Mach. 52 (2), 157–167. https://doi.org/10.6041/j.issn.1000-1298.2021.02.014 (in Chinese).

Zhao, Y., Wang, G.Y., Huang, B., et al., 2014. Vortex motion and hydrodynamic characteristics in unsteady cavitating flows. Chin. J. Theor. Appl. Mech. 46 (2), 191–200. https://doi.org/10.6052/0459-1879-13-177 (in Chinese).

Zhao, H.R., Wang, F.J., Wang, C.Y., et al., 2021. Study on the characteristics of horn-like vortices in an axial flow pump impeller under off-design conditions. Eng. Appl. Comput. Fluid Mech. 15 (1), 1613–1628. https://doi.org/10.1080/19942060.2021.1985615.

Zhao, B.J., Han, L.Y., Liu, Y.L., et al., 2022. Effects of blade placement angle on internal vortex structure and impeller-guide vane adaptability in mixed-flow pumps. J. Drain. Irrigat. Machin. Eng. 40 (2), 109–114. https://doi.org/10.3969/j.issn.1674-8530.20.0269 (in Chinese).

Zhao, H.R., Wang, F.J., Wang, C.Y., et al., 2023. Generation mechanism and control methods of secondary flows in the impeller of axial flow pumps. Phys. Fluids 35 (6), 065127. https://doi.org/10.1063/5.0158612.